



AMERICAN METEOROLOGICAL SOCIETY

Monthly Weather Review

EARLY ONLINE RELEASE

This is a preliminary PDF of the author-produced manuscript that has been peer-reviewed and accepted for publication. Since it is being posted so soon after acceptance, it has not yet been copyedited, formatted, or processed by AMS Publications. This preliminary version of the manuscript may be downloaded, distributed, and cited, but please be aware that there will be visual differences and possibly some content differences between this version and the final published version.

The DOI for this manuscript is doi: 10.1175/MWR-D-12-00301.1

The final published version of this manuscript will replace the preliminary version at the above DOI once it is available.

If you would like to cite this EOR in a separate work, please use the following full citation:

Ruppert, J., R. Johnson, and A. Rowe, 2013: Diurnal Circulations and Rainfall in Taiwan during SoWMEX/TiMREX (2008). *Mon. Wea. Rev.* doi:10.1175/MWR-D-12-00301.1, in press.



1
2
3
4
5
6
7
8
9
10
11
12
13
14

Diurnal Circulations and Rainfall in Taiwan during SoWMEX/TiMREX (2008)

James H. Ruppert, Jr.¹ and Richard H. Johnson
Department of Atmospheric Science, Colorado State University, Fort
Collins, Colorado

Angela K. Rowe
Department of Atmospheric Sciences, University of Washington, Seattle,
Washington

¹ Corresponding author address: James H. Ruppert Jr., Department of Atmospheric Science, 1371 Campus Delivery, Fort Collins, CO 80523.
E-mail: ruppert@atmos.colostate.edu

Abstract

15
16
17 The diurnal cycle of the local circulation, rainfall, and heat and moisture budgets is
18 investigated in Taiwan's heavy rain ("Mei-yu") season using data from the 2008
19 Southwest Monsoon Experiment/Terrain-influenced Monsoon Rainfall Experiment
20 (SoWMEX/TiMREX). Comparisons are made between an undisturbed (UNDIST; 22–29
21 May) and disturbed period (DIST; 31 May–4 June). Many aspects of the diurnal
22 evolution in surface flows and rainfall were similar during both periods. At night and
23 during early-morning hours, the low-level southwesterly flow was deflected around
24 Taiwan's main topographic barrier, the Central Mountain Range (CMR), with rainfall
25 focused near areas of enhanced offshore confluence created by downslope and land
26 breeze circulations. During the day, the flow switched to onshore and upslope, rainfall
27 shifted inland, and deep convection developed along the coastal plains and windward
28 slopes. Atmospheric budget analysis indicates a day-to-evening transition of convective
29 structure from shallow to deep to stratiform. Evaporation associated with the
30 evening/nighttime stratiform precipitation likely assisted the nocturnal katabatic flow.

31 Though the flow impinging on Taiwan was blocked during both periods, a very
32 moist troposphere and strengthened low-level oncoming flow during DIST resulted in
33 more widespread and intense rainfall that was shifted to higher elevations, which
34 resembled a more weakly blocked regime. Correspondingly, storm cores were tilted
35 upslope during DIST, in contrast to the more erect storms characteristic of UNDIST.

36 There were much more lofted precipitation-sized ice hydrometeors within storms during
37 DIST, the upslope advection of which led to extensive stratiform rain regions overlying
38 the CMR peaks, and the observed upslope shift in rainfall.

40

41

1. Introduction

42 A strong diurnal pulsation of rainfall is connected to coastal regions and areas of sloped
43 topography in the tropics and subtropics, which are attended by prominent land/sea
44 breeze (LSB) and mountain/valley (MV) circulations. In the mountainous subtropical
45 island of Taiwan, rainfall is controlled throughout the year by such circulations, which
46 cause a pronounced diurnal oscillation in island-averaged low-level divergence (Johnson
47 and Bresch 1991; Chen et al. 1999; Kishtawal and Krishnamurti 2001; Kerns et al. 2010;
48 Lin et al. 2011). Great complexity is added to this system in the presence of monsoon
49 flow, which interacts with Taiwan's main topographic barrier, the Central Mountain
50 Range (CMR), to generate enhanced upstream convergence, barrier jets, offshore
51 rainbands, and lee vortices (Sun and Chern 1993; Li and Chen 1998; Yeh and Chen 2002;
52 Chen et al. 2004; Alpers et al. 2007; Yu and Lin 2008; Yu and Hsieh 2009). The manner
53 in which such features interact with the diurnal cycle needs further investigation, as these
54 two major aspects of Taiwan meteorology have been studied quite separately to date.
55 Improved understanding of the diurnal cycle of rainfall and relationships with flow
56 blocking was a core focus of the Southwest Monsoon Experiment/Terrain-influenced
57 Monsoon Rainfall Experiment (SoWMEX/TiMREX; Jou et al. 2011), which was
58 conducted during the 2008 heavy rain season in Taiwan (the *Mei-yu* or plum-rain season).

59 The *Mei-yu* season in Taiwan is the mid-May–mid-June period in which the
60 stable northeasterly winter monsoon transitions to the convectively unstable
61 southwesterly summer monsoon (Chen 1983; Chen 1993; Ding and Chan 2005). During
62 this season, a pronounced zone of low-level convergence and cyclonic shear will

63 periodically develop where these flows meet (the Mei-yu front), in connection with a
64 strengthened southwesterly low-level jet, amplified upper-level flow pattern, and
65 deepened East Asian monsoon trough (Chen 1983; Chen 1993; Chen et al. 2008). During
66 such *disturbed conditions*, this subtropical Mei-yu frontal system, which typically forms
67 north of Taiwan, can shift southwards into the Taiwan area and provide an effective
68 triggering mechanism for copious rainfall through mesoscale convective systems (MCSs)
69 that spawn and propagate eastward along its ~zonally oriented strip of barotropic
70 vorticity (Chen 1983; Chen et al. 2008; Lai et al. 2011). Lai et al. (2011) documented a
71 case from SoWMEX/TiMREX in which a MCS propagated offshore from southern
72 China and organized into an intense mesoscale convective vortex (MCV), aided by
73 stretching from deep convection along the frontal vorticity line. Vigorous convection
74 was favored downshear (east) of the MCV where northward advection of unstable low-
75 level air was enhanced, which caused heavy rainfall along the Mei-yu front and inland
76 flooding as it propagated eastward across southern Taiwan. Shallow, rain-generated
77 coastal boundaries unrelated to the Mei-yu front can also be important for heavy rainfall
78 during the Mei-yu-season (Davis and Lee 2012; Xu et al. 2012). While these boundaries
79 typically exhibit virtual temperature contrasts of only 2~3°C (cooler over land), they
80 enhance near-shore and offshore convergence enough to invigorate free convection in the
81 moist impinging southwesterly flow (Davis and Lee 2012; Xu et al. 2012).

82 Johnson and Bresch (1991) describe the diurnal cycle characteristic of Mei-yu
83 *undisturbed periods* – periods when the Mei-yu front is either not present or is situated
84 north of Taiwan, rainfall is reduced, and relatively uniform southwesterly flow impinges
85 on Taiwan. They used observations from the 1987 Taiwan Area Mesoscale Experiment

86 (TAMEX; Kuo and Chen 1990), and found that daytime sea breezes and anabatic flows
87 strengthened in the late morning and early afternoon as deep convection increased along
88 the coastal plains and western foothills of the CMR. Convection transitioned to
89 stratiform rainfall by evening as evaporation-enhanced katabatic flows and land breezes
90 developed. Finally, rainfall maximized offshore during the overnight and early-morning
91 hours. Subsequent studies have employed satellite data as well as the dense rain gauge
92 network in Taiwan to corroborate these findings and extend the analysis to other seasons
93 (Chen et al. 1999; Kishtawal and Krishnamurti 2001; Kerns et al. 2010; Lin et al. 2011).
94 These and other studies have primarily focused on undisturbed periods or seasonal
95 means. It is important to assess the role and character of the diurnal cycle in more
96 disturbed environments when conditions are more conducive for heavy rainfall, such as
97 when the subtropical Mei-yu front develops and shifts southward over Taiwan.

98 A major factor in the distribution and intensity of rainfall in Taiwan relates to the
99 effects of topography. Figure 1 provides a topographic map of Taiwan showing the
100 coastal plains in the west and the steep slopes of the CMR. Note that the CMR slopes
101 extend down nearly to the eastern coastline, resulting in an east–west asymmetry in the
102 distribution of lowlands surrounding to the CMR. From theory, the Burger number B can
103 be used to diagnose the “hydrodynamic steepness” of the mountain barrier, where $B =$
104 HN_m / fL , H is ridge height, N_m is the subsaturated moist Brunt Väisälä frequency, f is the
105 Coriolis parameter, and L is flow-parallel mountain half-width. When $B \ll 1$, the slope
106 is mild and the flow remains in quasi-geostrophic balance, and when $B \gg 1$, the slope is
107 significant and ageostrophic flows divert around the barrier (Baines 1987; Pierrehumbert
108 and Wyman 1985; Smolarkiewicz et al. 1988; Overland and Bond 1995). Using

109 approximations for Taiwan ($H \sim 2$ km, $L \sim 50$ km, $N_m \sim 10^{-2} \text{ s}^{-1}$, and $f \sim 10^{-4} \text{ s}^{-1}$; Li and
110 Chen 1998), $B = 4$, suggesting that the CMR is a hydrodynamically steep barrier that will
111 block the flow. For any characteristic wind speed $U \leq 20 \text{ m s}^{-1}$, the Froude number $\text{Fr} =$
112 $U / N_m H$ is sub-unity (using the approximations above), suggesting that the kinetic energy
113 of the flow is small relative to the potential energy required to surmount the barrier;
114 hence the flow is diverted (Smolarkiewicz et al. 1988). While utility of a saturated Brunt
115 Väisälä frequency is apt in saturated conditions (e.g., Durran and Klemp 1982), saturation
116 is limited to the scale of individual cloud systems when the prevailing upstream flow is
117 subsaturated as it was during SoWMEX/TiMREX; therefore, Fr as defined above is
118 appropriate for diagnosing the predominate flow characteristics around Taiwan (Baines
119 1987; Smolarkiewicz et al. 1988; Carbone et al. 1995; Li and Chen 1998; Chen and Lin
120 2005; Hughes et al. 2009; Miglietta and Rotunno 2009).

121 Blocked flows around Taiwan result in areas of enhanced low-level convergence
122 and rainfall surrounding the island; for example, quasi-stationary convective rainbands
123 frequently appear offshore of southeastern Taiwan all-year-round in connection with flow
124 blocking (Yu and Jou 2005; Yu and Hsieh 2009; Alpers et al. 2010). The pre-Mei-yu-
125 frontal heavy rainfall events in northwestern Taiwan offer another example of orographic
126 rainfall enhancement (Li and Chen 1998; Yeh and Chen 2002; Wang et al. 2005). The
127 Big Island of Hawaii provides a related example in which diurnal and orographic
128 processes interact to produce a prominent arch-shaped rainband upwind of the island
129 (Smolarkiewicz et al. 1988; Carbone et al. 1995). Initially, evaporative cooling from
130 diurnal rainfall in the elevated terrain generates a nocturnal katabatic, offshore flow. The
131 rainband forms offshore where this flow converges with the impinging stable trade wind.

132 Finally, the rainband moves onshore as daytime heating drives a reversal to onshore,
133 upslope flow. In addition to the general enhancement of rainfall by orography, rainfall
134 distribution can be complicated by the flow–microphysical interactions that occur when
135 widespread deep convection is present (Jiang 2003; Chen and Lin 2005; Miglietta and
136 Rotunno 2009; Murphy and Businger 2011).

137 In the present study, the SoWMEX/TiMREX enhanced sounding network is
138 employed to describe the diurnal cycle of mesoscale diurnal circulations and heat and
139 moisture budgets (i.e., latent heating) over Taiwan, with comparison between undisturbed
140 and disturbed conditions. Johnson and Bresch (1991) is the only prior study to do
141 similar, though the sounding network they employed (TAMEX) had marginal spatial
142 coverage and diurnal variability during disturbed periods was not discussed. New
143 estimates of the vertical and horizontal distributions of diabatic heating will provide a
144 basis for validation and comparison with numerical simulations of the diurnal cycle over
145 Taiwan.

146

147 2. Datasets and Methodology

148 *a. Gridded dataset*

149 Previous studies have successfully employed objective interpolation procedures to
150 sounding datasets from a number of tropical and monsoon field campaigns, e.g., TOGA
151 COARE, SCSMEX, and NAME, and obtained reliable results confirmed by analysis of
152 independent datasets (Lin and Johnson 1996; Johnson and Ciesielski 2002; Ciesielski et
153 al. 2003; Johnson et al. 2010). A similar approach is followed in this study, which allows

154 dynamical relationships to emerge from observations with minimized influence from
155 model information.

156 A gridded analysis (denoted INTERP) is generated on a 0.25° mesh from 18°N ,
157 112°E to 28°N , 124°E with 40 vertical levels (surface and 50–1000 hPa at 25 hPa
158 increments) by running observations through the multiquadric interpolation scheme of
159 Nuss and Titley (1994). The main sampling period of SoWMEX/TiMREX (special
160 observing period; SOP) spanned 15 May–26 June 2008, during which time a dense
161 network of rawinsondes, radars, wind profilers, and surface stations was deployed in and
162 around Taiwan (Jou et al. 2011). The SoWMEX/TiMREX sounding network was
163 composed of 13 sites, including land stations in and bordering Taiwan and stations in the
164 northern South China Sea (SCS) and Taiwan Strait (Fig. 1). Six-hourly soundings
165 were taken at most sites during the SOP, with three-hourly soundings during a ~weeklong
166 enhanced observing period (EOP) from late May–early June. During the EOP the Mei-yu
167 front amplified and shifted southward into the northern SCS (Lai et al. 2011; Davis and
168 Lee 2012). Sixteen dropsonde missions (yielding 190 soundings) were also carried out
169 during this EOP and a later active period. Ciesielski et al. (2010) describes the extensive
170 SoWMEX/TiMREX sounding dataset and quality control procedures, which resulted in
171 substantial improvements in the humidity field (removal of dry biases).

172 The observations employed in INTERP are listed in Table 1. Operational
173 soundings from China are included to supplement the SoWMEX/TiMREX sounding
174 dataset away from Taiwan (yielding a total of 32 sounding sites). Quick Scatterometer
175 (QuikSCAT) sea surface wind data were filtered to 0.25° spacing prior to the
176 interpolation, with all rain- and land-contaminated data excluded. Similar to previous

177 studies employing this technique (e.g., Johnson and Ciesielski 2002), inclusion of data
178 from operational 0.5° NCEP Global Forecast System (GFS) analyses at several points
179 outside of the main sounding network (Fig. 1) was necessary to minimize the effects of
180 extrapolation into data-sparse regions (particularly east of Taiwan, where flow blocking
181 can substantially modify the far flow fields). The impacts were primarily on mean
182 magnitudes, while the day-to-day and diurnal variability was primarily reflecting
183 observations. This is discussed further in the Appendix. Due to sampling errors in
184 sounding observations (Mapes et al. 2003), 3-day running means are applied to SOP time
185 series based on INTERP fields to increase statistical significance. Additional details of
186 the multiquadric procedure can be found in Ciesielski et al. (2003).

187

188 *b. Independent datasets*

189 To diagnose characteristics of afternoon thunderstorms during focal periods of the study,
190 two cross sections are generated using data from the National Center for Atmospheric
191 Research (NCAR) S-band, Doppler, polarimetric radar (S-Pol) that was deployed in
192 southwestern coastal Taiwan during SoWMEX/TiMREX (22.53N, 120.43E; Fig. 1).
193 Full-volume 360° surveillance scans allowed for rain mapping to a maximum range of
194 150 km along the western slopes of the CMR, enabling comparisons and coordination
195 with the neighboring Pingdong sounding station. Quality control of the S-Pol dataset
196 followed the methods of Lang et al. (2007). The corrected suite of polarimetric variables
197 (cf. Rowe et al. 2011, 2012) were gridded to Cartesian coordinates at 1-km horizontal and
198 0.5-km vertical grid spacing using the program REORDER (Mohr et al. 1986). A
199 hydrometeor identification (HID) algorithm was applied to infer the dominant

200 hydrometeor types at each grid point, including drizzle (DZ), rain (RA), dry snow (DS),
201 wet snow (WS), vertical ice (IC), low-density graupel (LG), high-density graupel (HG),
202 and hail (HA). This HID algorithm, which employed the gridded polarimetric variables
203 and temperature profiles from the Pingdong sounding station (Fig. 1), is based on the
204 fuzzy logic methodology of Liu and Chandrasekar (2000), and is described in detail by
205 Tessendorf et al. (2005).

206 Rainfall from the Quantitative Precipitation Estimation and Segregation Using
207 Multiple Sensors (QPESUMS) dataset is employed, which combines information from
208 Taiwan's network of operational radars (that is, not S-Pol) and rain gauges operated by
209 the Central Weather Bureau of Taiwan, and is available hourly at 0.0125° spacing over
210 and immediately surrounding Taiwan. Taiwan's operational rain gauge network is quite
211 dense (Chen et al. 1999; Kishtawal and Krishnamurti 2001; Kerns et al. 2010), thus
212 providing a good check on radar-derived rainfall. A concern in the QPESUMS dataset is
213 offshore negative rainfall biases related to radar beam-blockage, particularly near
214 southeastern Taiwan (Chang et al. 2009). As will be shown, the resulting errors in
215 southeastern Taiwan are often obvious, particularly during rainy periods; the discounting
216 of data where this occurs is therefore straightforward. The Tropical Rainfall Measuring
217 Mission (TRMM; Kummerow et al. 2000) 3B42v6 rainfall dataset (Huffman et al. 2007)
218 is also employed, which is available three-hourly at 0.25° spacing. The TRMM 3B42v6
219 product (simply denoted TRMM, hereafter) includes infrared (IR) brightness temperature
220 data to fill in time gaps, leading to erroneous assignment of rainfall in areas of large non-
221 raining high clouds (Liu et al. 2007). This TRMM dataset is useful for the study,

222 however, in that it provides valuable information away from Taiwan where neither the
 223 rain gauge network nor radars do so.

224

225 *c. Diagnostic quantities*

226 Following Yanai et al. (1973), vertical profiles of the *apparent heat source* Q_1 and
 227 *apparent moisture sink* Q_2 are calculated, which enable diagnosis of precipitating systems
 228 from large-scale sounding measurements. These terms are defined as follows:

$$229 \quad Q_1 \equiv \frac{\partial \bar{s}}{\partial t} + \bar{\mathbf{v}} \cdot \nabla \bar{s} + \bar{\omega} \frac{\partial \bar{s}}{\partial p} = Q_R + L(\bar{c} - \bar{e}) - \frac{\partial \overline{\omega' s'}}{\partial p}, \quad (1)$$

$$230 \quad Q_2 \equiv -L \left(\frac{\partial \bar{q}}{\partial t} + \bar{\mathbf{v}} \cdot \nabla \bar{q} + \bar{\omega} \frac{\partial \bar{q}}{\partial p} \right) = L(\bar{c} - \bar{e}) + L \frac{\partial \overline{\omega' q'}}{\partial p} \quad (2)$$

231 where $s = c_p T + gz$ is dry static energy, \mathbf{v} is horizontal wind, ω is vertical pressure
 232 velocity, Q_R is radiative heating, L is latent heat of vaporization, c is condensation rate, e
 233 is evaporation rate, q is water vapor mixing ratio, c_p is specific heat of dry air, T is
 234 temperature, g is gravitational acceleration, z is height, the overbar denotes an area
 235 average, and the prime represents the eddy component. The Lagrangian tendencies of
 236 heat (s) and moisture (q), i.e., the left-hand side of (1) and (2), are directly calculated
 237 from INTERP. Q_1 and Q_2 are then divided by c_p to express them in temperature
 238 tendencies. Divergence δ is vertically mass-balanced by assuming adiabatic flow at the
 239 tropopause and using a constant divergence correction (O'Brien 1970). δ is vertically
 240 integrated to diagnose ω . The lower boundary for ω is determined by calculating slope
 241 flow (Luo and Yanai 1983).

242 Estimated rainfall rate is calculated for INTERP by vertically integrating Q_2 and
243 adding surface latent heat flux LH to close the moisture budget (Yanai et al. 1973). LH
244 estimates were obtained from Year of Tropical Convection (YOTC) European Centre for
245 Medium-Range Weather Forecasts analyses (Waliser et al. 2012). Inaccuracies in
246 budget-derived rainfall can result from errors in Q_2 (the moisture and/or kinematic
247 fields), poor LH estimates from YOTC, and neglect of water vapor storage in clouds
248 (McNab and Betts 1978; Johnson 1980).

249

250 3. SoWMEX/TiMREX Overview

251 As demonstrated by a time series of daily-mean rainfall averaged over Taiwan (Fig. 2),
252 rainfall varied substantially through the SOP, with approximately a week separating two
253 rainy (disturbed) periods (discussed below). INTERP exhibits wet biases early and late
254 in the SOP relative to QPESUMS (i.e., ending ~18 May and beginning ~17 June,
255 respectively). During these periods, the SoWMEX/TiMREX sounding network was not
256 in full operation (Ciesielski et al. 2010), and hence there was likely poor sampling of the
257 complex, blocked flow around Taiwan. However, apart from the 1–2-day rainfall delay
258 relative to QPESUMS evident during the two disturbed periods, INTERP properly
259 captures the rainfall magnitudes and general rainfall evolution.

260 Figure 3 provides SOP time–pressure sections of daily-mean fields averaged over
261 Taiwan from INTERP, including zonal and meridional flows u and v and relative
262 humidity RH. Onset of the low-level southwesterly flow occurred around 22 May, which
263 coincided with a period of deep moisture following passage of a 200-hPa trough (on ~19
264 May). Two subsequent moist periods can be noted, with progressively drier periods

265 separating them. Figure 4 provides SOP time–pressure sections of δ , ω , Q_1 , and Q_2 . The
266 three dry (undisturbed periods) can be identified in Figs. 2–4 by reduced rainfall and
267 tropospheric RH, abated tropospheric flow, and predominant subsidence (mid–late May,
268 6~12 June, and 17~25 June). The third undisturbed period is an exception, which
269 exhibits weak rising motion, heating, and drying in Fig. 4. With such dry conditions aloft
270 (Fig. 3) and negligible rainfall in QPESUMS (Fig. 2), however, it can be assumed that the
271 rising motion, heating and drying are likely erroneous. This demonstrates that reduction
272 in sounding frequency and coverage during this period degraded the ability of the
273 SoWMEX/TiMREX sounding network to accurately capture the environment. The third
274 and driest undisturbed period coincides with a switch to 200-hPa northeasterly flow,
275 reflecting a northward shift of the 200-hPa Asian anticyclone.

276 The early- and mid-June disturbed periods were characterized by deep moisture,
277 strengthened tropospheric flow, and deep rising motion, heating, and drying (Figs. 3 and
278 4). Low-level cooling (negative Q_1) during the early-June disturbed period indicates
279 more stratiform rainfall compared with that in mid-June, which was apparently more
280 convective in nature. During the ~weeklong period preceding the early-June disturbed
281 period, strengthened westerly momentum descended from the upper troposphere (Fig. 3).
282 Tropospheric moistening then commenced (~29 May), suggesting establishment of the
283 southwesterly moisture stream (Ding and Chan 2005). Heavy rainfall developed in
284 Taiwan around 2 June (Figs. 2 and 4), by which time the Mei-yu front had developed and
285 shifted southward into the northern SCS where it remained through 5 June. Passage of a
286 200-hPa trough (with $u > 20 \text{ m s}^{-1}$) can be noted during this disturbed period (Fig. 3).
287 Chen (1993) found that Mei-yu fronts during TAMEX were associated with an

288 amplifying wave pattern in which the Asian anticyclone shifted northward over the
 289 Tibetan Plateau and the midlatitude westerly jet shifted southward to the Taiwan area.
 290 As discussed by Lai et al. (2011), a MCV spun up along the Mei-yu front during this
 291 active period and impacted southern Taiwan on 5 June. The mid-June disturbed period
 292 was unrelated to a Mei-yu front. MCSs first propagated across southern Taiwan, leaving
 293 a residual cold pool (14–15 June). A quasi-stationary MCS then developed offshore
 294 where moist southwesterly flow (Fig. 3) overrode this cold pool (15–16 June). Davis and
 295 Lee (2012) and Xu et al. (2012) discuss this case in detail.

296 Figure 5 provides time series of three-hourly and daily-mean measurements of
 297 sensible heat SH , T , LH , and q from the National Taiwan University (NTU) experimental
 298 forest flux site at Pingdong (Fig. 1; note that data are only available through mid-June).
 299 The magnitude of the diurnal cycle in SH evolves in concert with daily mean SH , e.g.,
 300 note decreases in both in late May related to increasing cloud cover with the southward-
 301 advancing Mei-yu front (Davis and Lee 2012). Similar evolution can be noted in T .
 302 Diurnal variability in T and SH persists through the early-June disturbed period, though it
 303 is reduced relative to the undisturbed periods. There is a steady increase in daily-mean
 304 and three-hourly LH with the progression of the Mei-yu season, reflecting moistening
 305 soil and vegetation green-up. Daily-mean q increases similarly, with notable jumps near
 306 monsoon onset and the start of the early-June disturbed period.

307 Provided in Figure 6 (top) are hourly T' (Taiwan-averaged T with SOP-mean
 308 removed) and slope flow U_{SLOPE} , defined as the surface flow component parallel to the
 309 surface height gradient, averaged over Taiwan (positive values denote upslope).² T' and
 310 U_{SLOPE} are calculated using observations from 55 quality-controlled surface stations in

² U_{SLOPE} is directly proportional to surface ω (described in Section 2).

311 Taiwan, following multiquadric interpolation (Nuss and Titley 1994) onto a 0.25° mesh.
312 In the lower panel, Taiwan-averaged QPESUMS rainfall is provided in hourly and three-
313 day running mean form.

314 Diurnal variation of U_{SLOPE} reflects the combined LSB and MV circulations (Fig.
315 6). Morning and afternoon perturbations to the regular diurnal cycle are likely related to
316 LSB fronts and convective outflows. T' and U_{SLOPE} reach maximum (~ 13 local time, LT)
317 and minimum (~ 03 LT) near the same time each day. Rainfall maximizes between 15
318 and 18 LT on most days throughout the SOP, demonstrating the strong coupling of
319 rainfall to the diurnal cycle. There is a several-hour offset between maximum T' and
320 U_{SLOPE} and peak rainfall on many days (e.g., 26 May), as noted in other studies (Johnson
321 and Bresch 1991; Kerns et al. 2010). Similar to T and SH from the Pingdong flux tower
322 (Fig. 5), rainfall activity (i.e., smoothed rainfall) and magnitude of the diurnal cycle in T'
323 and U_{SLOPE} are inversely related. However, while the diurnal cycle in T' and U_{SLOPE} is
324 greatly reduced during the two June disturbed periods, afternoon rainfall peaks are still
325 observed on most days. Furthermore, the early-June disturbed period exhibits a regular,
326 albeit reduced, diurnal cycle in T' and U_{SLOPE} .

327

328 4. Analysis of the Diurnal Cycle

329 Next, compositing is employed to compare the diurnal cycles of two periods of the SOP
330 (indicated in Fig. 6) – an undisturbed period “UNDIST” spanning 22–29 May (8 days),
331 and a disturbed period “DIST” spanning 31 May–4 June (5 days). The two June
332 undisturbed periods were excluded from UNDIST composites because very dry
333 conditions aloft resulted in suppressed rainfall (Figs. 3 and 6). The mid-June disturbed

334 period was excluded from DIST composites since it was characterized by substantial
335 synoptic variability (Fig. 6; Davis and Lee 2012; Xu et al. 2012), offering poor
336 persistence for a composite analysis. 5 June is also excluded from DIST composites
337 since much of the circulation and rainfall activity on that day was related to the
338 propagation of an intense MCV across the island (Lai et al. 2011).

339 UNDIST is a characteristic period of monsoonal moist southwesterly flow in a
340 subsidence-dominated, dry troposphere (Figs. 2 and 3), with a pronounced diurnal cycle
341 in T , slope flows, and rainfall (Fig. 6). DIST is characteristically different from UNDIST
342 in that there is much heavier rainfall (Fig. 2), strengthened southwesterly monsoon flow
343 overriding a Mei-yu front in the northern SCS, and deep moisture in connection with the
344 upstream moistening by frontal lifting and associated convection (Fig. 3). Diurnal
345 variability evidently persisted through DIST (Fig. 6). The goal herein is to address how
346 the differing environmental characteristics between the two periods are manifested in the
347 diurnal cycle of rainfall and circulations.

348 Compositing is performed by averaging variable time series for UNDIST and
349 DIST as a function of time-of-day. Six-hourly composites are generated for UNDIST,
350 and three-hourly composites for DIST, since it coincided with the EOP. Figure 7
351 provides time series of diurnal composite rainfall from INTERP and QPESUMS for
352 UNDIST and DIST. During UNDIST, QPESUMS rainfall ramps up slowly through
353 morning, with intensification around noon related to the onset of convection (Johnson
354 and Bresch 1991; Kishtawal and Krishnamurti 2001; Kerns et al. 2010). With six-hourly
355 sampling, INTERP cannot properly resolve this intensification or the exact timing of the
356 peak, though the general evolution and maximum value has merit.

357 Afternoon rainfall in QPESUMS is doubled during DIST (compare ~20 to 40 mm
358 day⁻¹; Fig. 7, bottom), with rainfall observed throughout the day. QPESUMS rainfall
359 intensifies around noontime, similar to UNDIST, likely reflecting the onset of deep
360 convection. The absence of nighttime and morning rainfall in INTERP seems dubious.
361 Evidence suggests that the magnitudes of mean Q_1 and Q_2 in INTERP may have slight
362 errors owing to difficulty sampling the complex orographically enhanced gradients in
363 temperature and moisture across the CMR (where there are little data; Fig. 1) and
364 between Taiwan and the surrounding region (M. Toy 2012, personal discussion). In
365 particular, horizontal gradients in s and q along the coastal plain are not well represented
366 owing to the lack of sounding data over the interior of Taiwan, such that terrain-induced
367 subsidence warming and drying are not offset by horizontal advection. However,
368 INTERP properly captures the diurnal rainfall evolution. Three-hourly sampling during
369 this period provides more detailed diurnal structure. Morning intensification of and peak
370 rainfall occur slightly earlier than QPESUMS (~one time step in INTERP). This bias
371 may relate to water storage in developing clouds, which would be reflected as rainfall in
372 the moisture budget (McNab and Betts 1978; Johnson 1980).

373

374 *a. Undisturbed period (UNDIST): 22–29 May 2008*

375 The flow is predominant southwesterly during UNDIST, according to a map of UNDIST
376 mean surface streamlines and QPESUMS and TRMM rainfall (Fig. 8). However, there is
377 an area of diffluence and confluence upstream and downstream of Taiwan, respectively,
378 related to flow blocking by Taiwan (Section 1). A mean upstream sounding for UNDIST
379 from Dongsha Island (location indicated in Fig. 8; sounding not shown) indicates that Fr

380 ~ 0.3 in the 700–950-hPa layer, with layer-mean flow $U \sim 8 \text{ m s}^{-1}$; thus, the low-level
381 ambient flow is blocked by Taiwan. Consistent with a blocked-flow regime, rainfall
382 maximizes upstream of the terrain peaks (i.e., along the coastal plains and lower CMR
383 slopes) and along and offshore of the northwestern coast (Hughes et al. 2009). There is
384 very little rainfall southwest of Taiwan. With regard to the area of TRMM rainfall east of
385 Taiwan, which is barely hinted at by QPESUMS, there are neither upper-air data nor
386 other observations to verify its existence; hence, it will not be discussed in this study.

387 Figure 9 presents maps of UNDIST diurnal composite rainfall (three-hourly) and
388 surface flow patterns (six-hourly). Diurnal surface flow anomalies (Fig. 9a) are
389 generated by removing the UNDIST mean from the diurnal composites (Fig. 9b). The
390 diurnal flow anomalies demonstrate a pronounced reversal over Taiwan's slopes and over
391 the Taiwan Strait, which reflects the oscillating LSB and MV circulations (Fig. 6). The
392 flows retaining the composite mean (Fig. 9b) demonstrate how this evolution manifests in
393 the low-Fr ambient flow. From 02–08 LT, streamlines divert around Taiwan, with
394 enhanced streamline confluence in the Taiwan Strait in connection with nocturnal
395 downslope and offshore flows in Taiwan and China (Fig. 9a). At 05 LT (near sunrise),
396 coastal rainbands can be noted around the island, with a marked example near
397 northwestern-coastal Taiwan (Fig. 9a). This pronounced rainband resembles the
398 orographically enhanced convective rainbands often observed southeast of Taiwan (Yu
399 and Jou 2005; Alpers et al. 2007; Yu and Lin 2008) and the arc-shaped rainband observed
400 in the blocked trade-wind flow upstream of the Big Island of Hawaii (Smolarkiewicz et
401 al. 1988). From 05–11 LT, showers move onshore and increase in coverage over Taiwan
402 as anomalous downslope and offshore flows weaken (Fig. 9a). By 14 LT, there is

403 pronounced anomalous onshore and upslope flow (Fig. 9a) and rainfall has increased in
404 intensity and coverage over the coastal plains and windward slopes, reflecting
405 development of deep convection (Kishtawal and Krishnamurti 2001). Whereas the
406 southwesterly streamlines bow slightly around Taiwan in morning and overnight, they
407 direct inland and traverse the CMR at 14 LT (Fig. 9b). Rainfall coverage increases
408 further by 17 LT. By 20 LT, rainfall has substantially dissipated, and the flow has
409 returned to downslope (Fig 9b). Rainfall is organized in close alignment with the Taiwan
410 coast at 23 LT (Fig. 9a), suggesting the development of sea-breeze fronts.

411 Taiwan area-averaged vertical profiles of δ , ω , Q_1 , and Q_2 for UNDIST are shown
412 in Fig. 10 as both period averages and diurnal composite time series. The lowest levels in
413 these profiles (i.e., below 800 hPa) mostly reflect coastal data, since inland points are
414 below ground. Also, since the CMR is displaced east-of-center in Taiwan (Fig. 1),
415 characteristics of the western slopes dominate these averages. This spatial bias is
416 discussed further in the Appendix section. In the mean there is pronounced low-level
417 divergence and mid-level convergence, which is associated with subsidence from ~900
418 hPa to mid levels and weak rising motion aloft. Lower tropospheric divergence and
419 sinking motion are consistent with the upwind splitting of blocked, low-Fr flow, as
420 discussed earlier. The vertical patterns in mean Q_1 , and Q_2 – warming and drying above
421 cooling and moistening – suggest that stratiform rain is the predominant form of
422 precipitation (Houze 1982; Johnson 1984). However, evidence suggests that the
423 magnitudes of mean Q_1 and Q_2 may have slight errors associated with unresolved
424 horizontal gradients in temperature and moisture in and around Taiwan (see earlier
425 discussion on this). In spite of these potential errors, the diurnal evolution depicted in

426 Fig. 10 is sound and consistent with previous studies of diurnal rainfall in Taiwan (e.g.,
427 Johnson and Bresch 1991; Kishtawal and Krishnamurti 2001). For example, upper-level
428 divergence coincides with rising motion, warming, and drying through most of the
429 column around 14 LT, demonstrating that afternoon precipitation is predominantly
430 convective (Fig. 10, lower panels). The timing of deep convection is consistent with the
431 diurnal rainfall evolution during UNDIST based on both INTERP and independent
432 observations (Figs. 7 and 9).

433 In the early morning (02 LT), sinking motion and low-level divergence can be
434 noted, which are associated with the land breeze and katabatic flow. By mid-morning a
435 shallow layer of convergence develops near the surface associated with the sea breeze
436 and anabatic flow, which follows a low-level divergence maximum that ascends with
437 time into the afternoon. This convergence–divergence pattern is consistent with
438 development of a shallow cumulus field in response to island heating. Similar results
439 were found over the mountains of northwestern Mexico during the North American
440 Monsoon Experiment (Johnson et al. 2010). Low-level heating (08 LT) precedes low-
441 level rising motion, presumably as a result of eddy heat flux convergence in the boundary
442 layer after sunrise. Deep convection develops by 14 LT, as indicated by divergence
443 around 300-hPa and upper-level rising motion, heating, and drying. This coincides with
444 the development of upslope flow and inland rainfall (Figs. 9 and 10). A pronounced
445 stratiform rainfall pattern develops by afternoon (20 LT), as indicated by strengthened
446 upper-tropospheric divergence, convergence around the 0°C level, and lower- (upper-)
447 tropospheric sinking (rising) motion (Johnson and Bresch 1991; Kishtawal and
448 Krishnamurti 2001). In noting that this stratiform rain transition coincides with the

449 development of downslope flows (Fig. 9b), a connection can be inferred between evening
450 rainfall evaporation (i.e., lower-tropospheric cooling and moistening) and the onset of
451 nocturnal katabatic regime, similar to the Big Island of Hawaii (Carbone et al. 1995).

452

453 *b. Disturbed period (DIST): 31 May–4 June 2008*

454 A map of mean surface streamlines and rainfall for DIST (Fig. 11) clearly depicts the
455 Mei-yu front, which separates southwesterly summer monsoon flow from northeasterly
456 flow to the north. There is a clear concentration of rainfall along and south of the frontal
457 confluence line, which is largely associated with eastward-propagating frontal MCSs
458 (Chen 1983; Lai et al. 2011; Davis and Lee 2012). Several southwesterly streamlines can
459 be noted in Taiwan, reflecting the shallow nature of the Mei-yu front (Chen 1983).
460 Because of more widespread rainfall during DIST, the QPESUMS issue related to radar
461 beam-blockage offshore of southern Taiwan is clearly visible in Fig. 11.

462 In Taiwan, rainfall is shifted higher along the windward slopes relative to
463 UNDIST (Figs. 8 and 11). Based on a mean sounding for DIST from Dongsha Island
464 (not shown), $Fr \sim 0.6$ over 700–950 hPa, with $U \sim 14 \text{ m s}^{-1}$ in the layer. The upslope
465 shift in rainfall relative to UNDIST is consistent with larger U and Fr , which suggests
466 reduced flow blocking (though Fr remains < 1 ; Hughes et al. 2009). With a very moist
467 troposphere (Fig. 3) and larger U and Fr , however, the atmosphere is conducive to more
468 vigorous and/or widespread deep convection during this period. The importance of
469 differing convective storm characteristics from UNDIST in more weakly blocked flow
470 will be assessed in Section 5.

471 Figure 12 provides maps of diurnal composite rainfall and surface flows (now
472 three-hourly) for DIST. In the anomaly flows (Fig. 12a), there is a change from weak
473 downslope and offshore flow over Taiwan during the night (most pronounced at 23 LT)
474 to upslope flow and confluence in the CMR by midday (14 LT), which coincides with
475 heavy inland rainfall (peak rainfall coverage is again at 17 LT). Similar to UNDIST,
476 rainfall appears to move inland from the west coast through morning (08–11 LT) before
477 intensifying substantially over the high terrain as afternoon convection develops (11–17
478 LT; Fig. 7). The flows with composite mean retained (Fig. 12b) depict interesting
479 relationships between the Mei-yu northeasterly flow and diurnal flows in Taiwan. A
480 cyclonic circulation is evident at 23 LT where downslope and offshore flows drain into
481 the northeasterly flow near southwestern Taiwan. This circulation can also be noted from
482 05–08 LT, during which period it shifts eastward in connection with rainfall
483 intensification over southwestern Taiwan (Fig. 12a). This circulation no longer appears
484 once the streamlines around Taiwan transition to onshore and upslope by afternoon.

485 To assess how persistent this circulation is, as well as the other features in Fig. 12,
486 Fig. 13 is provided with individual morning (05 LT) and afternoon (17 LT) rainfall and
487 surface flow maps on six of the EOP days (31 May–5 June; recall that DIST only
488 includes 31 May–4 June). While day-to-day variability is indeed pronounced, there is
489 persistence of some features. On several mornings, the aforementioned circulation
490 appears with confluence southwest of Taiwan, which resembles a lee vortex in the
491 northeasterly monsoon flow. In the afternoons, in contrast, the flow is more often
492 directed upslope, rainfall is increased over land, and the circulation is usually absent
493 (with the exception of the intense MCV of 5 June). No studies, to our knowledge, have

494 documented a diurnal circulation feature during Mei-yu disturbed periods. Thus, the
495 representativeness of these composites needs to be tested by future studies.

496 Figure 14 presents Taiwan area-averaged diurnal composite vertical profiles of δ ,
497 ω , Q_1 , and Q_2 for DIST. The mean profiles are qualitatively similar to those during
498 UNDIST (Fig. 10), with stratiform-like structure in vertical motion. As discussed
499 previously, the magnitudes of Q_1 and Q_2 may have small errors in their means associated
500 with unresolved gradients across the CMR and between Taiwan and the surrounding
501 region. The diurnal evolution, however, depicts a sound evolution that is consistent with
502 previous studies (e.g., Johnson and Bresch 1991) and the rainfall maps presented earlier.
503 For instance, note strong afternoon (14–17 LT) deep convection as indicated by
504 divergence near 200 hPa and rising motion, warming, and drying throughout the column,
505 which coincides with peak rainfall over the CMR (Figs. 7 and 12). Also note the
506 separation of midlevel Q_1 and Q_2 peaks, indicating upward transport of eddy heat flux
507 and hence vigorous deep convection (Yanai et al. 1973). An ascending divergence
508 maximum can be noted (near 800 hPa at 08 LT) in connection with shallow rising motion
509 and heating preceding deep convection, indicating a deepening shallow cumulus field
510 through morning. By afternoon (20 LT), a stratiform pattern of elevated rising motion,
511 heating, and drying is evident. This diurnal evolution from shallow cumulus to deep
512 convection to stratiform rain is qualitatively similar to UNDIST (Fig. 10), though the
513 signal of afternoon deep convection is much more pronounced, and three-hourly
514 sampling during the EOP provides improved detail.

515

516 5. Discussion

517 In this study the diurnal cycle during two periods of SoWMEX/TiMREX (2008) has been
518 described – one undisturbed (UNDIST; 22–29 May) and one disturbed (DIST; 31 May–4
519 June). UNDIST was characterized by relatively uniform southwesterly flow, a dry
520 midtroposphere (Fig. 3), and predominant subsidence (Fig. 4). In association with
521 reduced cloudiness (Fig. 5), there was a strong diurnal cycle in slope flows and rainfall
522 (Fig. 6), with rain peaking in the afternoon over the coastal plains and lower foothills of
523 western Taiwan (Fig. 9). The diurnal cycle in slope flows and rainfall remained
524 important during DIST (Figs. 7, 12, and 14), in spite of strengthened southwesterly flow,
525 a moist troposphere (Fig. 3), and a nearby Mei-yu front attended by heavy rainfall (Fig.
526 11).

527 A contrasting aspect between DIST and UNDIST is that peak rainfall was shifted
528 upslope during DIST relative to UNDIST (Figs. 8 and 11). Fr was larger during DIST in
529 connection with stronger oncoming lower-tropospheric flow, though Fr remained < 1
530 during both periods. Larger Fr is consistent with reduced flow blocking, in which rainfall
531 is expected to be a stronger function of terrain slope (Hughes et al. 2009). In the more
532 disturbed environment during DIST, however, flow–microphysical interactions might
533 have become important with more widespread convection (Jiang 2003; Chen and Lin
534 2005; Miglietta and Rotunno 2009; Murphy and Businger 2011). Storm microphysical
535 characteristics are discussed next.

536 Figure 15 provides west–east radar cross sections of reflectivity and hydrometeor
537 identification (HID) for two precipitating systems characteristic of UNDIST and DIST
538 (see Section 2b for procedures), which are located north of Pingdong (Fig. 1). The most

539 obvious difference between the two precipitating systems in Fig. 15 is their horizontal
540 extent. While both clearly depict deep convection, with vertically oriented cores of ≥ 50
541 dBZ peaking just below the 0°C level (due to the melting of falling graupel), the
542 UNDIST case is more isolated, as was characteristic of diurnal convection during these
543 more undisturbed days (Rowe 2011). The system during DIST (31 May), in contrast,
544 features a more strongly upslope-tilted convective core and a region of elevated graupel
545 of 25–30 km in extent, reflecting a large stratiform region stretching downstream of the
546 system's convective core. The presence of a strongly tilted updraft and large adjoining
547 stratiform region is consistent with the near-saturated environment and strengthened
548 cross-ridge southwesterly flow during DIST (Fig. 3), which aided the lofting of liquid
549 hydrometeors above the 0°C level, and hence the production of precipitation-sized ice
550 hydrometeors over the higher terrain. Murphy and Businger (2011) documented a similar
551 process in convective storms along the steep slopes of Oahu, Hawaii, a flooding event in
552 which rainfall was similarly maximized over the highest terrain peaks.

553 To summarize the key characteristics of the diurnal cycle discussed in this study
554 and the storm-scale processes described above, schematic diagrams of early-morning and
555 afternoon flow and rainfall patterns in Taiwan are provided for UNDIST and DIST in
556 Fig. 16. During the early-morning hours in UNDIST (DIST), the southwesterly
557 (northeasterly) flow was diverted around Taiwan while the flow within Taiwan was
558 predominately downslope and offshore. Early-morning rainfall during both periods was
559 primarily offshore surrounding Taiwan. During the early-morning in DIST there was a
560 lee vortex southwest of Taiwan where downslope and offshore flow drained into the post-
561 frontal northeasterly flow. Rainfall was present along the Mei-yu front in the northern

562 SCS throughout the day during DIST, with an area of enhanced rainfall just east of the
563 aforementioned early-morning circulation (suggesting the possible influence of
564 propagating MCVs in the composite; Lai et al. 2011). In the afternoon during both
565 periods, the ambient flow switched to onshore and upslope as convection developed
566 along the windward slopes. The circulation present during early-morning in DIST was
567 absent in the afternoon after the flow switched to onshore and upslope.

568 Afternoon rainfall was focused along the coastal plains and lower foothills during
569 UNDIST, while maximum rainfall during DIST was maximized in the higher terrain (Fig.
570 16). Strengthened flow during DIST resulted in more weakly blocked flow, strongly
571 upslope-tilted convective storm cores, and more lofted precipitation-sized ice
572 hydrometeors. These ice hydrometeors were advected over the higher terrain, leading to
573 extensive stratiform regions and the upslope shift in peak rainfall. UNDIST, in contrast,
574 exhibited more isolated convection and more strongly blocked flow, resulting in rainfall
575 peaking farther upstream of the high CMR slopes.

576

577 6. Summary and Conclusions

578 The diurnal cycle of mesoscale circulations and rainfall has been described during an
579 undisturbed and disturbed period of the 2008 Terrain-influenced Monsoon Rainfall
580 Experiment (SoWMEX/TiMREX). This study attempts to improve the understanding of
581 diurnal variability in the presence of steep terrain, and sensitivity of the diurnal cycle to
582 the strongly varying large-scale environment during Taiwan's Mei-yu season. Results for
583 DIST and UNDIST are generally consistent with previous studies of the diurnal cycle in
584 Taiwan (Johnson and Bresch 1991; Chen et al. 1999; Kishtawal and Krishnamurti 2001;

585 Kerns et al. 2010; Lin et al. 2011). However, the enhanced sounding network during the
586 42-day SoWMEX/TiMREX experiment (13 sites, with three- to six-hourly sampling)
587 allowed us to examine these phenomena with unprecedented detail.

588 The principal findings of the study are summarized as follows:

- 589 • Interpolation of the SoWMEX/TiMREX observational datasets has yielded a
590 detailed gridded analysis, from which a range of diagnostic analyses and
591 modeling validation efforts can be carried out.
- 592 • The diurnal cycle of atmospheric heating and moistening over Taiwan and its
593 vicinity indicates an evolution from shallow cumulus to deep convection (08–14
594 LT) to stratiform rain by evening (20 LT). This evolution is observed in both
595 disturbed and undisturbed conditions.
- 596 • While the amplitude of diurnal circulations and rainfall activity varies (inversely;
597 Fig. 6) between undisturbed and disturbed conditions, the diurnal evolution in
598 surface flow and rainfall patterns is similar. During the day, offshore rainfall
599 shifts eastward toward the windward slopes of Taiwan as the flow switches to
600 onshore and upslope, and amplifies in the afternoon (14–17 LT) along the
601 windward slopes. In the evening, the flow in Taiwan switches to downslope and
602 offshore, and rainfall redevelops in areas of offshore confluence. The coincidence
603 of the switch from upslope to downslope flow with the evening transition to
604 stratiform rain suggests that rainfall evaporation may play a key role in initiation
605 of the nocturnal katabatic flow, similar to the Big Island of Hawaii (Carbone et al.
606 1995).

- 607 • Although the amplitude of local diurnal circulations is reduced during highly
608 disturbed periods, more favorable characteristics for heavy rainfall make the
609 environment particularly sensitive to these circulations, such that the diurnal
610 variability in rainfall during those periods remains large.
- 611 • A circulation resembling a lee vortex is noted during the disturbed period when
612 the ambient flow around Taiwan is northeasterly. This circulation appears near
613 southwestern Taiwan during the night and morning, resembling a lee vortex in the
614 northeasterly flow. The vortex disappears once the flow switches to onshore and
615 upslope. The circulation–rainfall relationship resembles that of a MCV.
- 616 • Location of peak rainfall relative to the topography is sensitive to both the nature
617 of convection and flow blocking. When the impinging flow is strong (e.g., 15 m
618 s⁻¹) and the troposphere is conducive to widespread, intense convective storms,
619 greater production of lofted ice hydrometeors and their subsequent advection can
620 lead to a shift in peak rainfall to higher elevations than during undisturbed
621 conditions.

622 While the results presented for an undisturbed period are consistent with prior
623 studies of the diurnal cycle in Taiwan, few studies have analyzed the diurnal cycle in
624 disturbed summer monsoon conditions. Thus, more years should be compiled to assess
625 the representativeness of the disturbed period results present herein. The sensitivity of
626 the location of peak rainfall relative to topographic barriers to ambient flow
627 characteristics (i.e., tropospheric flow strength and humidity) has very important forecast
628 implications for Taiwan, which is a densely populated country characterized by frequent
629 landslides during Mei-yu season. More detailed analysis of the properties of raining

630 systems during the Mei-yu season, such as their microphysical properties and evolution,
631 will enable improved understanding of these sensitivities. The S-Pol radar deployed
632 during SoWMEX/TiMREX provides a great opportunity to do so. Better understanding
633 of the key controls on orographic rainfall properties in this region will improve the ability
634 to predict potentially life-threatening summer monsoon rainfall events.

635

636 *Acknowledgments.*

637 The authors acknowledge Paul Ciesielski for operating the multiquadric interpolation
638 scheme, Dr. Po-Hsiung Lin of NTU for providing data from the NTU experimental forest
639 flux site at Pingdong, and the Central Weather Bureau of Taiwan for providing
640 QPESUMS data. Helpful comments from Paul Ciesielski, Drs. Steven Fletcher, Hsiao-
641 Wei Lai, Jenny Sun, and Hongli Wang, and Profs. Eric Maloney, V. Chandrasekar, and
642 Ben Jong-Dao Jou are greatly appreciated. Three anonymous reviewers are also
643 acknowledged for their comments, which substantially improved the study. This research
644 was supported by National Science Foundation Grant AGS-0966758.

645

646

APPENDIX

647 **Interpolated Analysis and Taiwan Area Averages**

648 Figure A1 provides UNDIST diurnal composite vertical profiles of Q_1 averaged over
649 Taiwan from three sources: INTERP, INTERP excluding GFS data, and GFS. The most
650 obvious feature in Fig. A1 is the gross overestimation of heating by GFS (relative to
651 INTERP), which would be reflected as overestimated rainfall through the Q_1 budget

652 (Yanai et al. 1973). Furthermore, the diurnal evolution in GFS strongly differs from the
653 other two datasets. The two versions of INTERP are very similar in diurnal evolution,
654 exhibiting daytime shallow-to-deep heating peaks followed by heating over cooling in
655 evening, indicating stratiform rain.

656 Figure A2 provides mean and diurnal time–pressure sections of divergence,
657 vertical motion, Q_1 , and Q_2 for UNDIST. The only difference from Fig. 10 is that these
658 fields are averaged over western Taiwan instead of the entire island (the dividing line is
659 indicated in Fig. 1). Comparison of Figs. 10 and A2 demonstrates that the patterns in
660 western Taiwan dominate the full Taiwan-averages. This owes to the geographical
661 arrangement in Taiwan, with the main geographic barrier being displaced east of center
662 (Fig. 1). A subtle difference between Figs. 10 and A2 is that afternoon convection (as
663 seen in rising motion, Q_1 , and Q_2) is slightly stronger in Fig. A2, which is consistent with
664 Figs. 8 and 9 showing greater rainfall in western Taiwan.

665

666 **References**

- 667 Alpers, W., J.-P. Chen, I-I. Lin, and C.-C. Lien, 2007: Atmospheric fronts along the east
668 coast of Taiwan studied by ERS synthetic aperture radar images. *J. Atmos. Sci.*, **64**, 922–
669 937.
- 670 ———, ———, C.-J. Pi, and I-I. Lin, 2010: On the origin of atmospheric frontal lines off the
671 east coast of Taiwan observed on spaceborne synthetic aperture radar Images. *Mon. Wea.*
672 *Rev.*, **138**, 475–496.
- 673 Baines, P. G., 1987: Upstream blocking and airflow over mountains. *Ann. Rev. Fluid*
674 *Mech.*, **19**, 75–97.
- 675 Carbone, R. E., W. A. Cooper, and W.-C. Lee, 1995: Forcing of flow reversal along the
676 windward slopes of Hawaii. *Mon. Wea. Rev.*, **123**, 3466–3480.
- 677 Chang, P.-L., P.-F. Lin, B. J.-D. Jou, and J. Zhang, 2009: An application of reflectivity
678 climatology in constructing radar hybrid scans over complex terrain. *J. Atmos. Oceanic*
679 *Technol.*, **26**, 1315–1327.
- 680 Chen, C.-S., W.-C. Chen, and W.-K. Tao, 2004: Characteristics of heavy summer rainfall
681 in southwestern Taiwan in relation to orographic effects. *J. Meteor. Soc. Japan*, **82**,
682 1521–1543.
- 683 Chen, G. T.-J., 1983: Observational aspects of the Mei-Yu phenomenon in subtropical
684 China. *J. Meteor. Soc. Japan*, **61**, 306–312.
- 685 ———, C.-C. Wang, and S.-W. Chang, 2008: A diagnostic case study of Mei-yu
686 frontogenesis and development of wavelike frontal disturbances in the subtropical
687 environment. *Mon. Wea. Rev.*, **136**, 41–61.

- 688 Chen, S.-H., and Y.-L. Lin, 2005: Effects of moist Froude number and CAPE on a
689 conditionally unstable flow over a mesoscale mountain ridge. *J. Atmos. Sci.*, **62**, 331–
690 350.
- 691 Chen, T.-C., M.-C. Yen, J.-C. Hsieh, R. W. Arritt, 1999: Diurnal and seasonal variations
692 of the rainfall measured by the Automatic Rainfall and Meteorological Telemetry System
693 in Taiwan. *Bull. Amer. Meteor. Soc.*, **80**, 2299–2312.
- 694 Chen, Y.-L., 1993: Some synoptic-scale aspects of the surface fronts over southern China
695 during TAMEX. *Mon. Wea. Rev.*, **121**, 50–64.
- 696 Ciesielski, P. E., R. H. Johnson, P. T. Haertel, and J. Wang, 2003: Corrected TOGA
697 COARE sounding humidity data: Impact on diagnosed properties of convection and
698 climate over the warm pool. *J. Climate*, **16**, 2370–2384.
- 699 ———, W.-M. Chang, S.-C. Huang, R. H. Johnson, B. J.-D. Jou, W.-C. Lee, P.-H. Lin, C.-
700 H. Liu, and J. Wang, 2010: Quality controlled upper-air sounding dataset for
701 SoWMEX/TiMREX: Development and corrections. *J. Atmos. Ocean. Tech.*, **27**, 1802–
702 1821.
- 703 Davis, C. A., and W.-C. Lee, 2012: Mesoscale analysis of heavy rainfall episodes from
704 SoWMEX/TiMREX. *J. Atmos. Sci.*, **69**, 521–537.
- 705 Ding, Y. H., and C. L. Chan, 2005: The East Asian summer monsoon: An overview.
706 *Meteor. Atmos. Phys.*, **89**, 117–142.
- 707 Durran, D. R., and J. B. Klemp, 1982: On the effects of moisture on the Brunt-Väisälä
708 frequency. *J. Atmos. Sci.*, **39**, 2152–2158.
- 709 Houze, R. A., Jr., 1982: Cloud clusters and large-scale vertical motions in the tropics. *J.*
710 *Meteor. Soc. Japan*, **60**, 396–410.

- 711 ———, 2012: Orographic effects on precipitating clouds. *Rev. Geophys.*, **50**, RG1001,
712 doi:10.1029/2011RG000365.
- 713 Huffman, G. J., and Coauthors, 2007: The TRMM multisatellite precipitation analysis
714 (TMPA): Quasi-global, multiyear, combined-sensor precipitation estimates at fine scales.
715 *J. Hydrometeor.*, **8**, 38–55.
- 716 Hughes, M., A. Hall, and R. G. Fovell, 2009: Blocking in areas of complex topography,
717 and its influence on rainfall distribution. *J. Atmos. Sci.*, **66**, 508–518.
- 718 Jiang, Q., 2003: Moist dynamics and orographic precipitation. *Tellus*, **55a**, 301–316,
719 doi:10.1034/j.1600-0870.2003.00025.x.
- 720 Johnson, R. H., 1980: Diagnosis of convective and mesoscale motions during Phase III of
721 GATE. *J. Atmos. Sci.*, **37**, 733–753.
- 722 ———, 1984: Partitioning tropical heat and moisture budgets into cumulus and mesoscale
723 components: Implications for cumulus parameterization. *Mon. Wea. Rev.*, **112**, 1590–
724 1601.
- 725 ———, and J. F. Bresch, 1991: Diagnosed characteristics of precipitation systems over
726 Taiwan during the May–June 1987 TAMEX. *Mon. Wea. Rev.*, **119**, 2540–2557.
- 727 ———, and P. E. Ciesielski, 2002: Characteristics of the 1998 summer monsoon onset over
728 the northern South China Sea. *J. Meteor. Soc. Japan*, **80**, 561–578.
- 729 ———, ———, T. S. L'Ecuyer, and A. J. Newman, 2010: Diurnal cycle of convection during
730 the 2004 North American Monsoon Experiment. *J. Climate*, **23**, 1060–1078.
- 731 Jou, B. J.-D., W.-C. Lee, and R. H. Johnson, 2011: An overview of SoWMEX/TiMREX.
732 *The Global Monsoon System: Research and Forecasts, 2nd Edition*, C.-P. Chang, et al.
733 Eds., World Scientific, 303–318.

- 734 Kerns, J. B. W., Y.-L. Chen, and M.-Y. Chang, 2010: The diurnal cycle of winds, rain,
735 and clouds over Taiwan during the Mei-Yu, summer, and autumn rainfall regimes. *Mon.*
736 *Wea. Rev.*, **138**, 497–516.
- 737 Kishtawal, C. M., and T. N. Krishnamurti, 2001: Diurnal variation of summer rainfall
738 over Taiwan and its detection using TRMM Observations. *J. Appl. Meteor.*, **40**, 331–344.
- 739 Kummerow, C., and Coauthors, 2000: The status of the Tropical Rainfall Measuring
740 Mission (TRMM) after two years in orbit. *J. Appl. Meteor.*, **39**, 1965–1982.
- 741 Kuo, Y.-H., and G. T.-J. Chen, 1990: The Taiwan Area Mesoscale Experiment
742 (TAMEX): An overview. *Bull. Amer. Meteor. Soc.*, **71**, 488–503.
- 743 Lai, H.-W., C. A. Davis, and B. J.-D. Jou, 2011: A subtropical oceanic mesoscale
744 convective vortex observed during SoWMEX/TiMREX. *Mon. Wea. Rev.*, **139**, 2367–
745 2385.
- 746 Lang, T. J., D. A. Ahijevych, S. W. Nesbitt, R. E. Carbone, S. A. Rutledge, and R.
747 Cifelli, 2007: Radar-observed characteristics of precipitating systems during NAME
748 2004. *J. Climate*, **20**, 1713–1733.
- 749 Li, J., and Y.-L. Chen, 1998: Barrier jets during TAMEX. *Mon. Wea. Rev.*, **126**, 959–
750 971.
- 751 Lin, P.-F., P.-L. Chang, B. J.-D. Jou, J. W. Wilson, and R. D. Roberts, 2011: Warm
752 season thunderstorm characteristics under weak synoptic-scale forcing over Taiwan
753 Island. *Wea. Forecasting*, **26**, 44–60.
- 754 Lin, X., and R. H. Johnson, 1996: Kinematic and thermodynamic characteristics of the
755 flow over the western Pacific warm pool during TOGA COARE. *J. Atmos. Sci.*, **53**, 695–
756 715.

- 757 Liu, C., E. J. Zipser, S. W. Nesbitt, 2007: Global distribution of tropical deep convection:
758 Different perspectives from TRMM infrared and radar data. *J. Climate*, **20**, 489–503.
- 759 Liu, H., and V. Chandrasekar, 2000: Classification of hydrometeors based on
760 polarimetric radar measurements: Development of fuzzy logic and neuro-fuzzy systems,
761 and in situ verification. *J. Atmos. Oceanic Technol.*, **17**, 140–164.
- 762 Luo, H., and M. Yanai, 1983: The large-scale circulation and heat sources over the
763 Tibetan Plateau and surrounding areas during the early summer of 1979. Part I:
764 Precipitation and kinematic analyses. *Mon. Wea. Rev.*, **111**, 922–944.
- 765 Mapes, B. E., P. E. Ciesielski, and R. H. Johnson, 2003: Sampling errors in rawinsonde-
766 array budgets. *J. Atmos. Sci.*, **60**, 2697–2714.
- 767 McNab, A. L., and A. K. Betts, 1978: A mesoscale budget study of cumulus convection.
768 *Mon. Wea. Rev.*, **106**, 1317–1331.
- 769 Miglietta, M. M., and R. Rotunno, 2009: Numerical simulations of conditionally unstable
770 flows over a mountain ridge. *J. Atmos. Sci.*, **66**, 1865–1885.
- 771 Mohr, C. G., L. J. Miller, R. L. Vaughan, and H. W. Frank, 1986: The merger of
772 mesoscale datasets into a common Cartesian format for efficient and systematic analyses.
773 *J. Atmos. Oceanic Technol.*, **3**, 143–161.
- 774 Murphy, M. J., and S. Businger, 2011: Orographic influences on an Oahu flood. *Mon.*
775 *Wea. Rev.*, **139**, 2198–2217.
- 776 Nuss, W. A., and D. W. Titley, 1994: Use of multiquadric interpolation for
777 meteorological objective analysis. *Mon. Wea. Rev.*, **122**, 1611–1631.
- 778 O'Brien, J. J., 1970: Alternative solutions to the classical vertical velocity problem. *J.*
779 *Appl. Meteor.*, **9**, 197–203.

- 780 Overland, J. E., and N. A. Bond, 1995: Observations and scale analysis of coastal wind
781 jets. *Mon. Wea. Rev.*, **123**, 2934–2941.
- 782 Pierrehumbert, R. T., and B. Wyman, 1985: Upstream effects of mesoscale mountains. *J.*
783 *Atmos. Sci.*, **42**, 977–1003.
- 784 Rowe, A. K., 2011: A polarimetric radar analysis of convection observed during NAME
785 and TiMREX. Ph.D. dissertation, Colorado State University (CSU), 246 pp. [Available
786 from CSU Libraries, <http://lib.colostate.edu/etd/>.]
- 787 ———, S. A. Rutledge, and T. J. Lang, 2011: Investigation of microphysical processes
788 occurring in isolated convection during NAME. *Mon. Wea. Rev.*, **139**, 424–443.
- 789 ———, ———, and ———, 2012: Investigation of microphysical processes occurring in
790 organized convection during NAME. *Mon. Wea. Rev.*, **140**, 2168–2187.
- 791 Smolarkiewicz, P. K., R. M. Rasmussen, and T. L. Clark, 1988: On the dynamics of
792 Hawaiian cloud bands: Island forcing. *J. Atmos. Sci.*, **45**, 1872–1905.
- 793 Sun, W.-Y., and J.-D. Chern, 1993: Diurnal variation of lee vortices in Taiwan and the
794 surrounding area. *J. Atmos. Sci.*, **50**, 3404–3430.
- 795 Tessendorf, S. A., L. J. Miller, K. C. Wiens, and S. A. Rutledge, 2005: The 29 June 2000
796 supercell observed during STEPS. Part I: Kinematics and microphysics. *J. Atmos. Sci.*,
797 **62**, 4127–4150.
- 798 Waliser, D. E., and Coauthors, 2012: The “year” of tropical convection (May 2008 to
799 April 2010): Climate variability and weather highlights. *Bull. Amer. Meteor. Soc.*, **93**,
800 1189–1218.

- 801 Wang, C.-C., G. T.-J. Chen, T.-C. Chen, and K. Tsuboki, 2005: A numerical study on the
802 effects of Taiwan topography on a convective line during the Mei-Yu season. *Mon. Wea.*
803 *Rev.*, **133**, 3217–3242.
- 804 Xu, W., E. J. Zipser, Y.-L. Chen, C. Liu, Y.-C. Liou, W.-C. Lee, and B. J.-D. Jou, 2012:
805 An orography-associated extreme rainfall event during TiMREX: Initiation, storm
806 evolution, and maintenance. *Mon. Wea. Rev.*, **140**, 2555–2574.
- 807 Yanai, M., S. Esbensen, and J. H. Chu, 1973: Determination of bulk properties of tropical
808 cloud clusters from large-scale heat and moisture budgets. *J. Atmos. Sci.*, **30**, 611–627.
- 809 Yeh, H.-C., and Y.-L. Chen, 2002: The role of offshore convergence on coastal rainfall
810 during TAMEX IOP 3. *Mon. Wea. Rev.*, **130**, 2709–2730.
- 811 Yu, C.-K., and B. J.-D. Jou, 2005: Radar observations of the diurnally forced offshore
812 convective lines along the southeastern coast of Taiwan. *Mon. Wea. Rev.*, **133**, 1613–
813 1636.
- 814 ———, and Y.-H. Hsieh, 2009: Formation of the convective lines off the mountainous
815 coast of southeastern Taiwan: A case study of 3 January 2004. *Mon. Wea. Rev.*, **137**,
816 3072–3091.
- 817 ———, and C.-Y. Lin, 2008: Statistical location and timing of the convective lines off the
818 mountainous coast of southeastern Taiwan from long-term radar observations. *Mon. Wea.*
819 *Rev.*, **136**, 5077–5094.
- 820

821 **List of Figures**

822 FIG. 1. Topography is gray-shaded every 400 m. The 2-km level is contoured. Polygons
 823 denote 11 of the 13 rawinsonde stations constituting the Southwest Monsoon
 824 Experiment/Terrain-influenced Monsoon Rainfall Experiment (SoWMEX/TiMREX)
 825 enhanced sounding network. Sites not shown are Dongsha Island, located to the
 826 southwest (shown in Fig. 8) and Laoag, Philippines, located south of Taiwan. The plus
 827 sign denotes the S-Pol radar station, situated in coastal Pingdong. The Xs denote three
 828 surrounding GFS data points incorporated in the interpolated analysis (INTERP). The
 829 dashed line represents the dividing line for an area average over western Taiwan
 830 (Appendix). The two solid lines north of Pingdong denote the transects for two west–
 831 east-oriented radar cross sections discussed later.

832 FIG. 2. SoWMEX/TiMREX special observing period (SOP) time series of rainfall (mm
 833 day⁻¹) averaged over Taiwan from INTERP and Quantitative Precipitation Estimation
 834 and Segregation Using Multiple Sensors dataset (QPESUMS). Rainfall is diagnosed for
 835 INTERP from the moisture budget, as described in Section 2c. The numbers in
 836 parentheses are SOP means. Gray shading denotes undisturbed periods. Rainfall
 837 estimates were smoothed using a 3-day running mean.

838 FIG. 3. SOP time–pressure sections averaged over Taiwan from INTERP (dates along
 839 abscissa axis), including daily-mean zonal wind u (top; m s⁻¹), meridional wind v
 840 (middle; m s⁻¹), and relative humidity RH, with respect to ice where temperature $T < 0^{\circ}\text{C}$
 841 (bottom; %). Fields were smoothed using a 3-day running mean.

842 FIG. 4. As in Fig. 3 except with divergence δ (top; 10^{-6} s^{-1}), vertical pressure velocity ω
 843 (second from top; hPa h^{-1}), apparent heat source Q_1 (third from top; K day^{-1}), and
 844 apparent moisture sink Q_2 (bottom; K day^{-1}).

845 FIG. 5. Time series of flux tower measurements from Pingdong (Fig. 1), with sensible
 846 heat flux SH (top; W m^{-2}), T (second from top; $^{\circ}\text{C}$), latent heat flux LH (third from top;
 847 W m^{-2}), and water vapor mixing ratio q (bottom; g kg^{-1}). Data are shown in both three-
 848 hourly (thin) and daily-mean form (thick). Abscissa tick marks are at local midnight.
 849 The time series ends in mid-June, after which point data are unavailable. Data provided
 850 courtesy of Dr. P.-H. Lin.

851 FIG. 6. Top: hourly time series of slope flow U_{SLOPE} (positive for upslope; m s^{-1}) and
 852 temperature deviation from SOP-mean T' ($^{\circ}\text{C}$). Both are averaged over Taiwan and
 853 generated from surface stations. 13 and 03 local time (LT) values are traced out with
 854 dotted lines. Bottom: hourly and smoothed (using a three-day running mean) QPESUMS
 855 rainfall (mm day^{-1}) averaged over Taiwan. Polygons denote the afternoon (15–18-LT)
 856 maximum rainfall each day. Abscissa tick marks are at local midnight. Gray shading
 857 denotes undisturbed periods. Black vertical lines denote the bounds of the selected
 858 undisturbed (UNDIST; 22–29 May) and disturbed (DIST; 31 May–4 June) periods for
 859 compositing.

860 FIG. 7. Time series of diurnal composite rainfall (mm day^{-1}) averaged over Taiwan for
 861 UNDIST (top) and DIST (bottom) from INTERP and QPESUMS. First numbers in
 862 parentheses are maximum values and second are samples per day.

863 FIG. 8. UNDIST mean surface streamlines from INTERP (mean and maximum domain
 864 wind speed values provided at bottom) and rainfall (mm day^{-1}). QPESUMS rainfall is

865 shaded (color scale at right), and TRMM rainfall is contoured at 5, 20, and 35 mm day⁻¹
 866 inside of the QPESUMS domain (gray rectangle) and shaded surrounding it. The red “X”
 867 marks Dongsha Island sounding station. Terrain is gray-shaded as in Fig 1.

868 FIG. 9. (a): UNDIST six-hourly diurnal surface flow anomalies (m s⁻¹; reference vector
 869 and maximum value provided at bottom-right) with three-hourly UNDIST composite
 870 QPESUMS rainfall (mm day⁻¹; scale at bottom). (b): UNDIST six-hourly diurnal
 871 composite surface streamlines (mean and maximum domain values provided at bottom-
 872 left) with QPESUMS rainfall [shaded according to the color bar in (a)]. LT is indicated
 873 in the upper-left of each panel.

874 FIG. 10. UNDIST composite vertical profiles from INTERP averaged over Taiwan in
 875 mean (top) and diurnal composite (bottom) form (six-hourly sampling). From left to
 876 right: δ (10⁻⁶ s⁻¹), ω (hPa h⁻¹), Q_1 (K day⁻¹), and Q_2 (K day⁻¹). The 0°C level is dashed.
 877 Abscissae are mean values (top) and LT (bottom). 02-LT values are repeated in diurnal
 878 profiles for continuity.

879 FIG. 11. As in Fig. 8 except for DIST.

880 FIG. 12. As in Fig. 9 except for DIST. Note that the rainfall scale is doubled relative to
 881 Fig. 9. Also, diurnal flows are provided at three-hourly frequency during DIST since it
 882 coincided with the EOP. The magenta “X” in (b) marks a circulation center.

883 FIG. 13. Surface streamlines and QPESUMS rainfall (mm day⁻¹; shaded) for morning
 884 (2100 UTC; 05 LT the next day) and afternoon (0900 UTC; 17 LT) on 31 May–5 June.
 885 Dates are indicated at the top-left of each panel, which pertain to UTC time.

886 FIG. 14. As in Fig. 10 except for DIST (with three-hourly sampling).

887 FIG. 15. West-to-east radar cross sections for UNDIST (1300 LT 25 May; top) and DIST
888 (1322 LT 31 May; bottom). Cross sections follow the transects shown in Fig. 1
889 (UNDIST: southernmost transect; DIST: northernmost transect). Abscissa axis is
890 distance from S-Pol radar (km), elevation is on ordinate axis (km), surface elevation is
891 contoured in a thick black line, and the approximate 0°C level is indicated by the thin
892 horizontal line at 5 km. Shown are reflectivity (dBZ; shaded; left panels) and
893 hydrometeor identification (HID; shaded; right panels), with reflectivity contoured at 0,
894 30, 40, and 50 dBZ (with 40- and 50-dBZ contours thickened). HID categories are
895 drizzle (DZ), rain (RN), dry snow (DS), wet snow (WS), vertical ice (IC), low-density
896 graupel (LG), high-density graupel (HG), and hail (HA).

897 FIG. 16. Schematic depiction of the diurnal cycle looking northeast over Taiwan during
898 the two SoWMEX/TiMREX (2008) periods analyzed in this study. The undisturbed
899 period (left; 22–29 May) was characterized by relatively uniform southwesterly
900 impinging flow, large-scale subsidence, and a dry mid/upper-troposphere over Taiwan.
901 During the disturbed period (right; 31 May–4 June), a surface Mei-yu front was situated
902 in the northern SCS, the impinging southwesterly flow overriding the front was stronger
903 and moister than UNDIST, and afternoon rainfall in Taiwan was heavier. Precipitation
904 cores are schematically depicted to exemplify characteristics of afternoon deep
905 convection along the western-coastal plains and windward slopes. Orange, red, and
906 magenta shading indicates radar reflectivity exceeding 30-, 40-, and 50-dBZ,
907 respectively. Asterisks represent ice hydrometeors. The blue lines indicate rainfall.
908 Surface streamlines are based on 02- (05-) LT and 14- (17-) LT diurnal composites for
909 morning and afternoon during UNDIST (DIST), respectively. Wind profiles are based on

910 UNDIST and DIST mean soundings from Dongsha Island (location indicated in Fig. 8;
911 half and full barbs denote 2.5 and 5 m s^{-1} , respectively). Vertical scale is exaggerated to
912 emphasize terrain, and wind profiles and schematic clouds are not to scale.

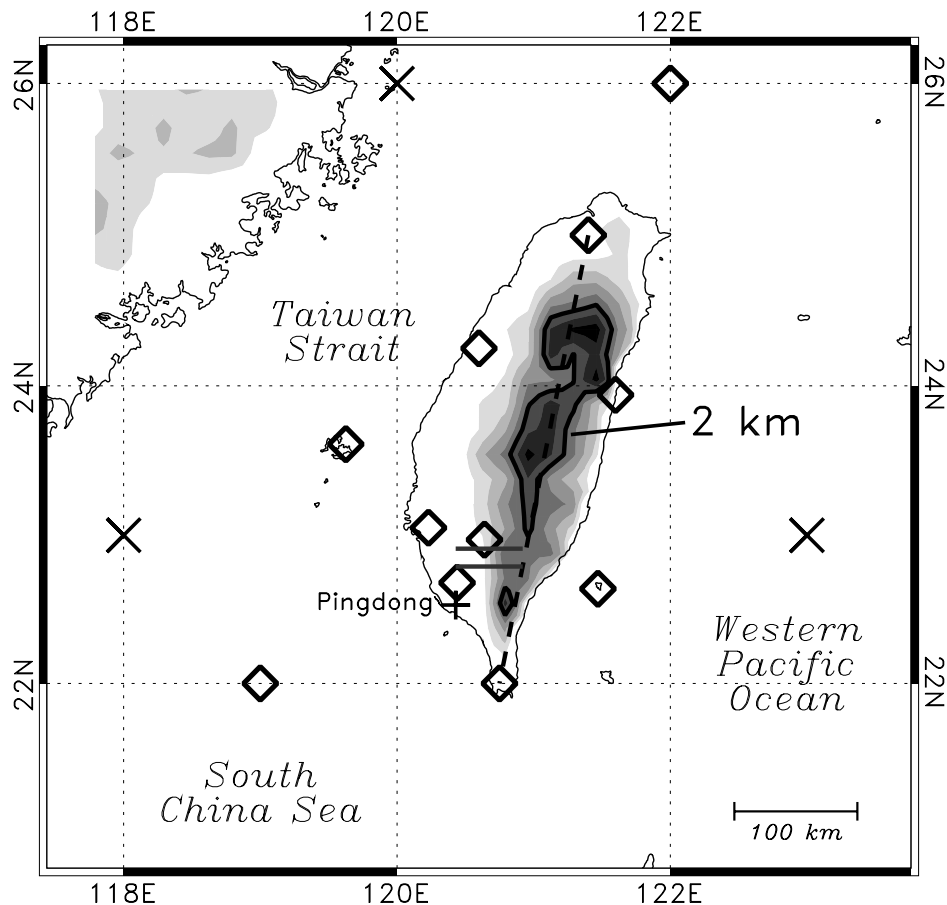
913 FIG. A1. UNDIST diurnal composite vertical profiles of Q_1 averaged over Taiwan from
914 INTERP (left), INTERP (excluding GFS data points; middle), and GFS (right).

915 FIG. A2. As in Fig. 10 except fields are averaged over western Taiwan (dividing line
916 indicated in Fig. 1).

917

918 TABLE 1. Observations used for the SoWMEX/TiMREX interpolated analysis (INTERP).

<i>Observation Type</i>	<i>Source</i>	<i>Approx. Quantity per Analysis</i>	<i>Daily Frequency in INTERP (during the EOP)</i>
Standard upper-air (up- and dropsonde)	SoWMEX/TiMREX and operational datasets (China and Taiwan)	10 000 (32 sondes)	4 (8)
Sea surface wind	Quick Scatterometer (QuikSCAT)	300–1 150	2 (2)
Standard surface	Taiwan's Central Weather Bureau (CWB) and Meteorological Assimilation Data Ingest System (MADIS)	200	4 (8)
Vertical profiler wind	CWB (operational)	60	4 (8)



920

921

922 FIG. 1. Topography is gray-shaded every 400 m. The 2-km level is contoured. Polygons

923 denote 11 of the 13 rawinsonde stations constituting the Southwest Monsoon

924 Experiment/Terrain-influenced Monsoon Rainfall Experiment (SoWMEX/TiMREX)

925 enhanced sounding network. Sites not shown are Dongsha Island, located to the

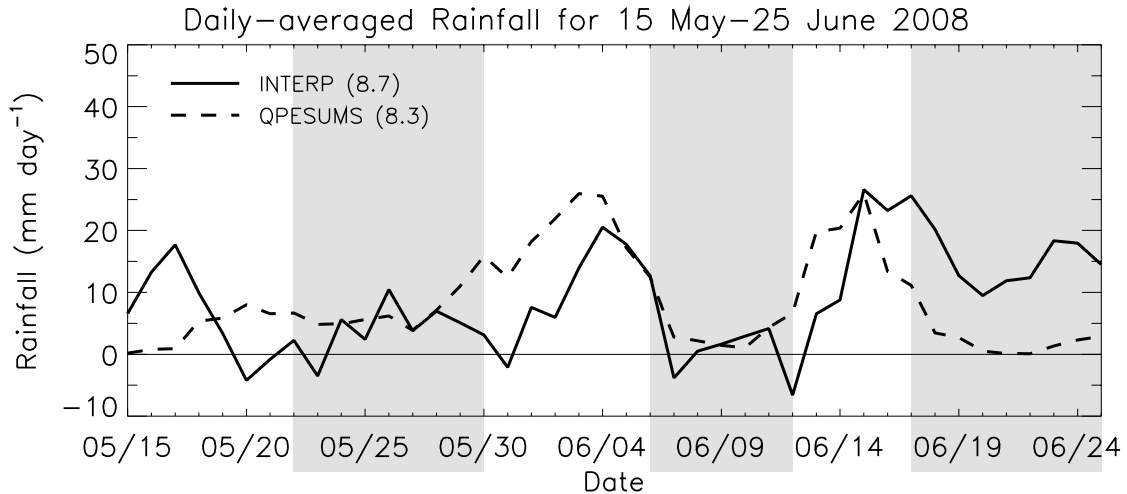
926 southwest (shown in Fig. 8) and Laoag, Philippines, located south of Taiwan. The plus

927 sign denotes the S-Pol radar station, situated in coastal Pingdong. The Xs denote three

928 surrounding GFS data points incorporated in the interpolated analysis (INTERP). The

929 dashed line represents the dividing line for an area average over western Taiwan

930 (Appendix). The two solid lines north of Pingdong denote the transects for two west–
931 east-oriented radar cross sections discussed later.
932

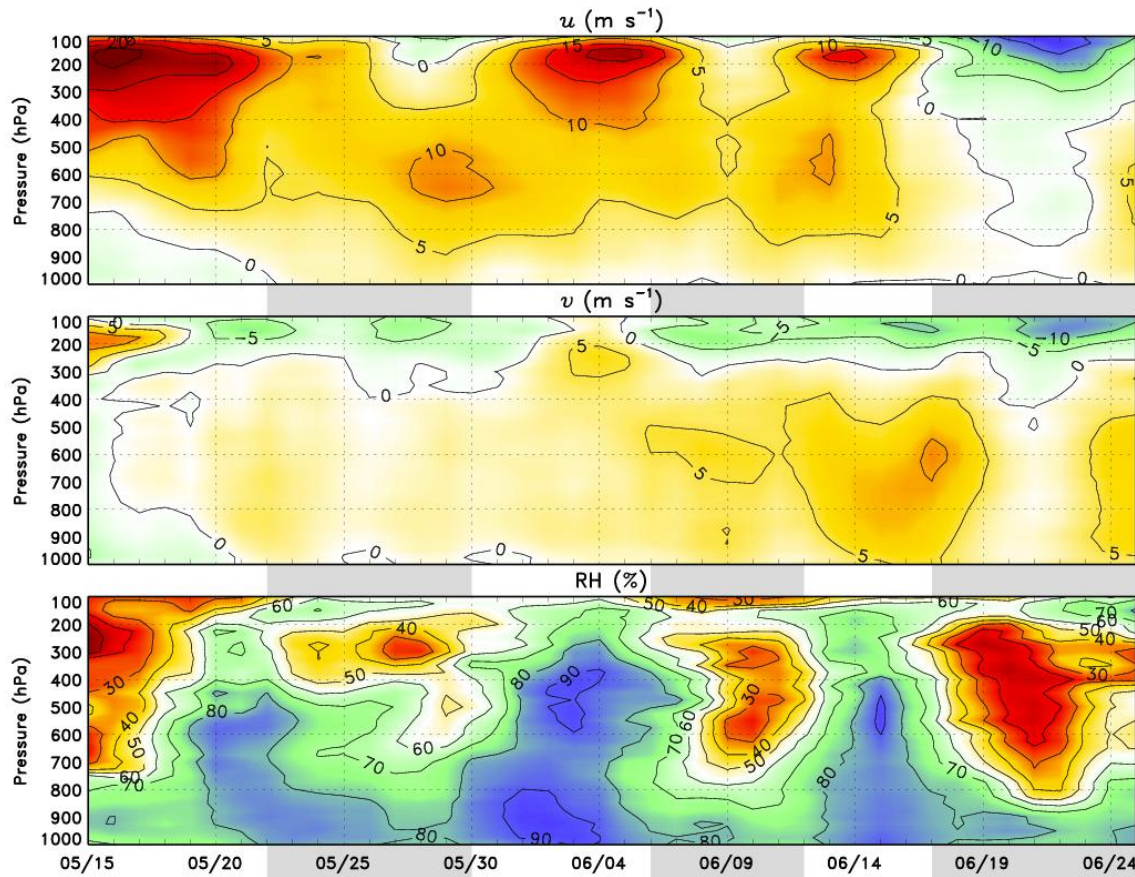


933

934

935 FIG. 2. SoWMEX/TiMREX special observing period (SOP) time series of rainfall (mm
 936 day⁻¹) averaged over Taiwan from INTERP and Quantitative Precipitation Estimation
 937 and Segregation Using Multiple Sensors dataset (QPESUMS). Rainfall is diagnosed for
 938 INTERP from the moisture budget, as described in Section 2c. The numbers in
 939 parentheses are SOP means. Gray shading denotes undisturbed periods. Rainfall
 940 estimates were smoothed using a 3-day running mean.

941



942

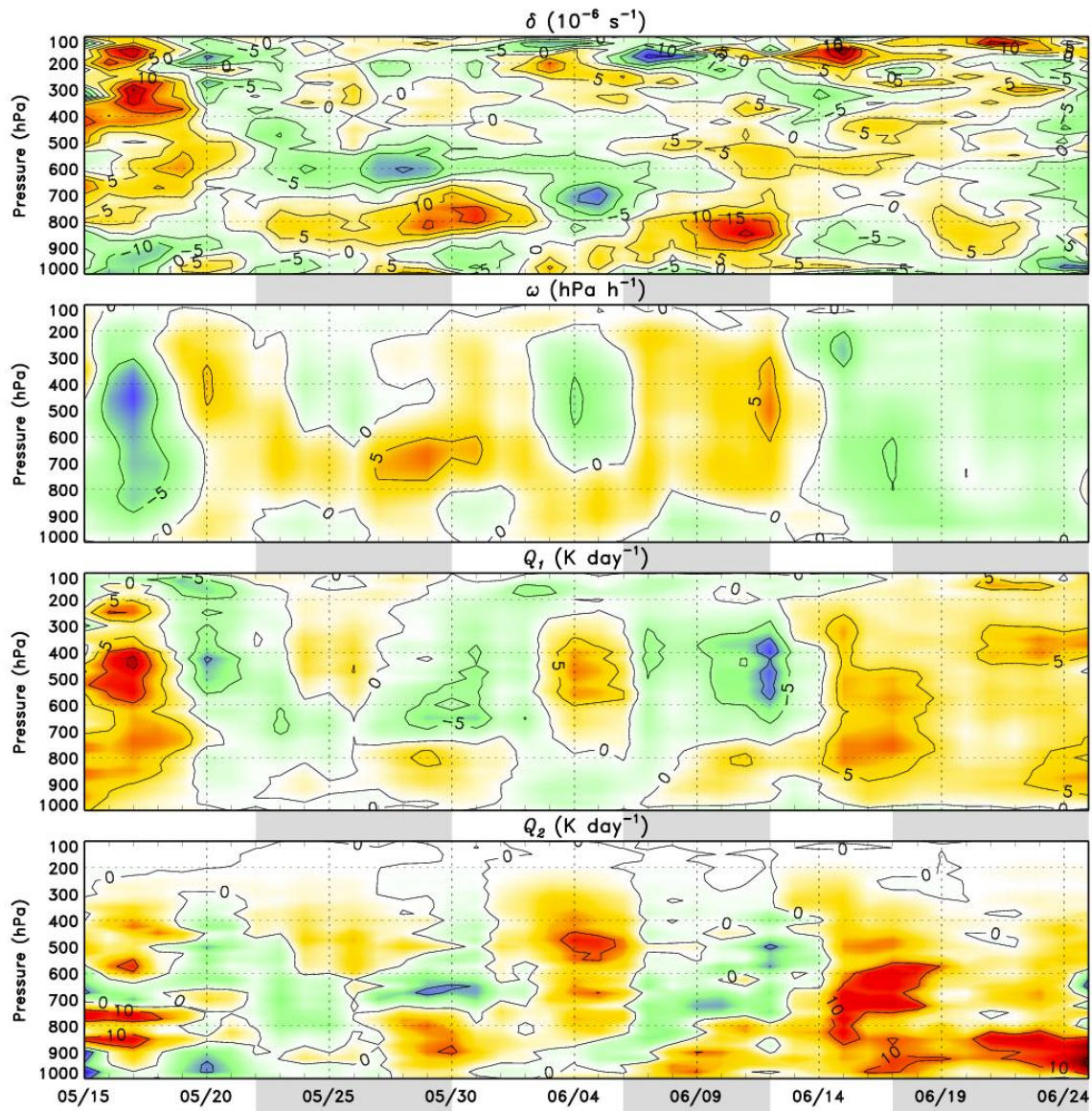
943

944 FIG. 3. SOP time–pressure sections averaged over Taiwan from INTERP (dates along

945 abscissa axis), including daily-mean zonal wind u (top; m s^{-1}), meridional wind v 946 (middle; m s^{-1}), and relative humidity RH, with respect to ice where temperature $T < 0^\circ\text{C}$

947 (bottom; %). Fields were smoothed using a 3-day running mean.

948

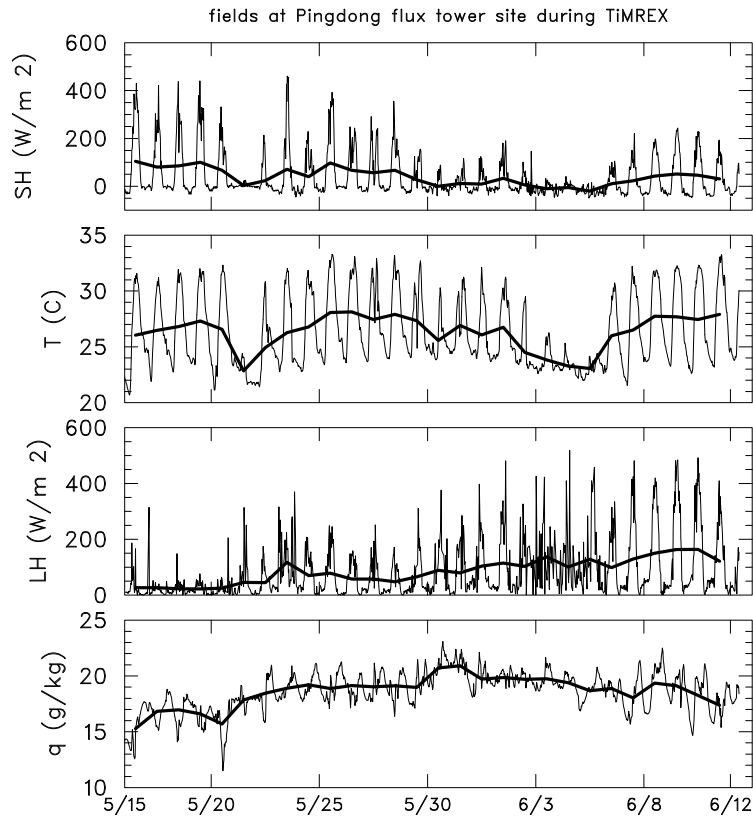


949

950

951 FIG. 4. As in Fig. 3 except with divergence δ (top; 10^{-6} s^{-1}), vertical pressure velocity ω 952 (second from top; hPa h^{-1}), apparent heat source Q_1 (third from top; K day^{-1}), and953 apparent moisture sink Q_2 (bottom; K day^{-1}).

954

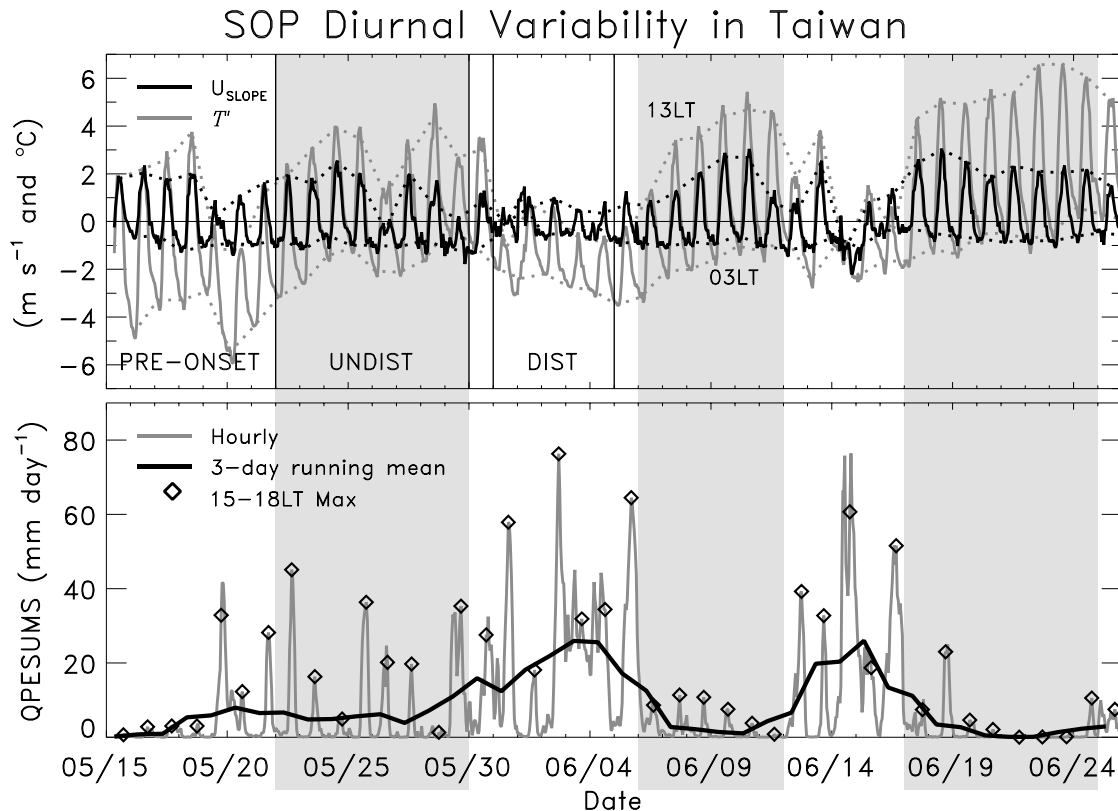


955

956

957 FIG. 5. Time series of flux tower measurements from the National Taiwan University
 958 (NTU) experimental forest flux site at Pingdong (Fig. 1), with sensible heat flux SH (top;
 959 W m^{-2}), T (second from top; $^{\circ}\text{C}$), latent heat flux LH (third from top; W m^{-2}), and water
 960 vapor mixing ratio q (bottom; g kg^{-1}). Data are shown in both three-hourly (thin) and
 961 daily-mean form (thick). Abscissa tick marks are at local midnight. The time series ends
 962 in mid-June, after which point data are unavailable. Data provided courtesy of Dr. P.-H.
 963 Lin at NTU.

964

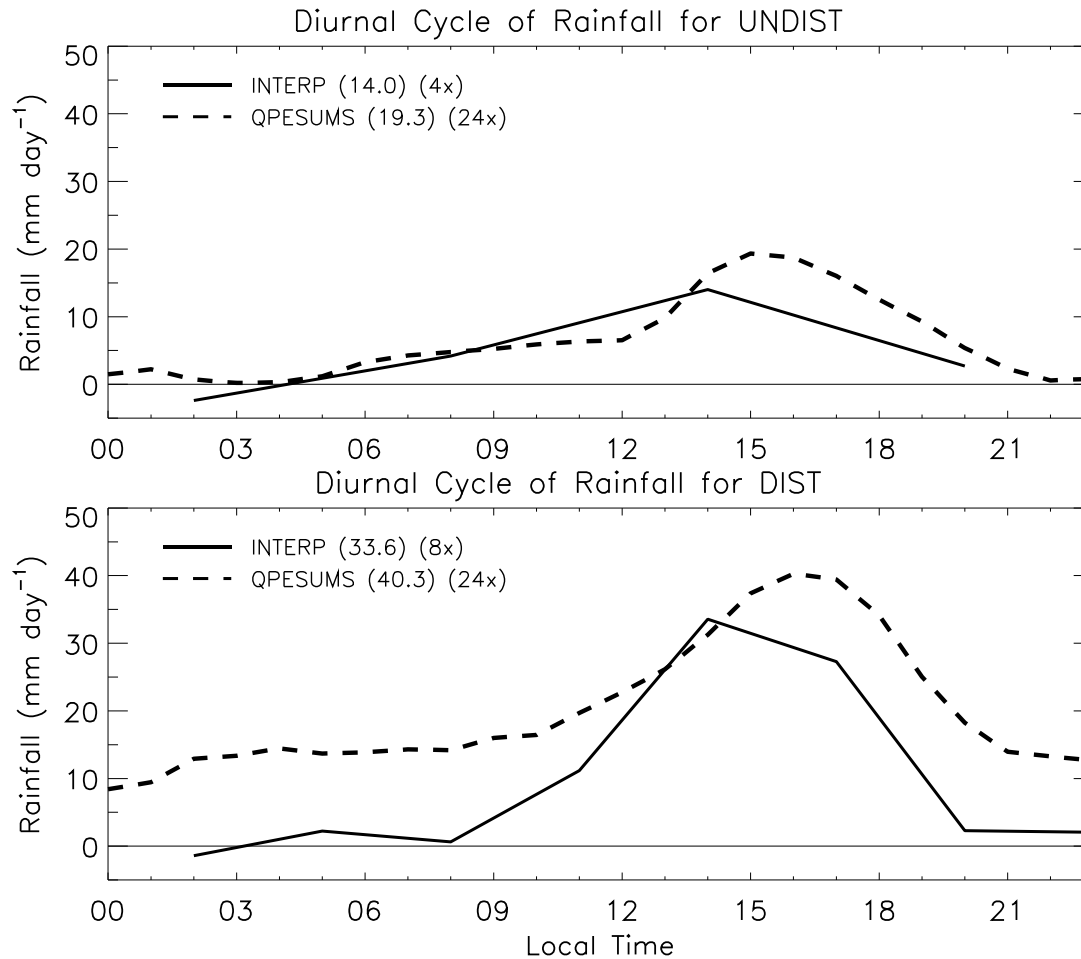


965

966

967 FIG. 6. Top: hourly time series of slope flow U_{SLOPE} (positive for upslope; m s^{-1}) and
 968 temperature deviation from SOP-mean T' ($^{\circ}\text{C}$). Both are averaged over Taiwan and
 969 generated from surface stations. 13 and 03 local time (LT) values are traced out with
 970 dotted lines. Bottom: hourly and smoothed (using a three-day running mean) QPESUMS
 971 rainfall (mm day^{-1}) averaged over Taiwan. Polygons denote the afternoon (15–18-LT)
 972 maximum rainfall each day. Abscissa tick marks are at local midnight. Gray shading
 973 denotes undisturbed periods. Black vertical lines denote the bounds of the selected
 974 undisturbed (UNDIST; 22–29 May) and disturbed (DIST; 31 May–4 June) periods for
 975 compositing.

976



977

978

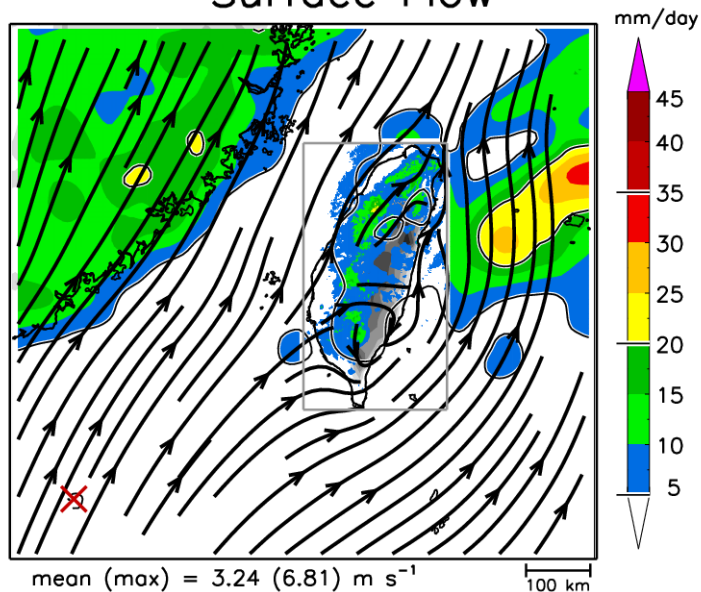
979 FIG. 7. Time series of diurnal composite rainfall (mm day⁻¹) averaged over Taiwan for

980 UNDIST (top) and DIST (bottom) from INTERP and QPESUMS. First numbers in

981 parentheses are maximum values and second are samples per day.

982

UNDIST Mean Rainfall and Surface Flow

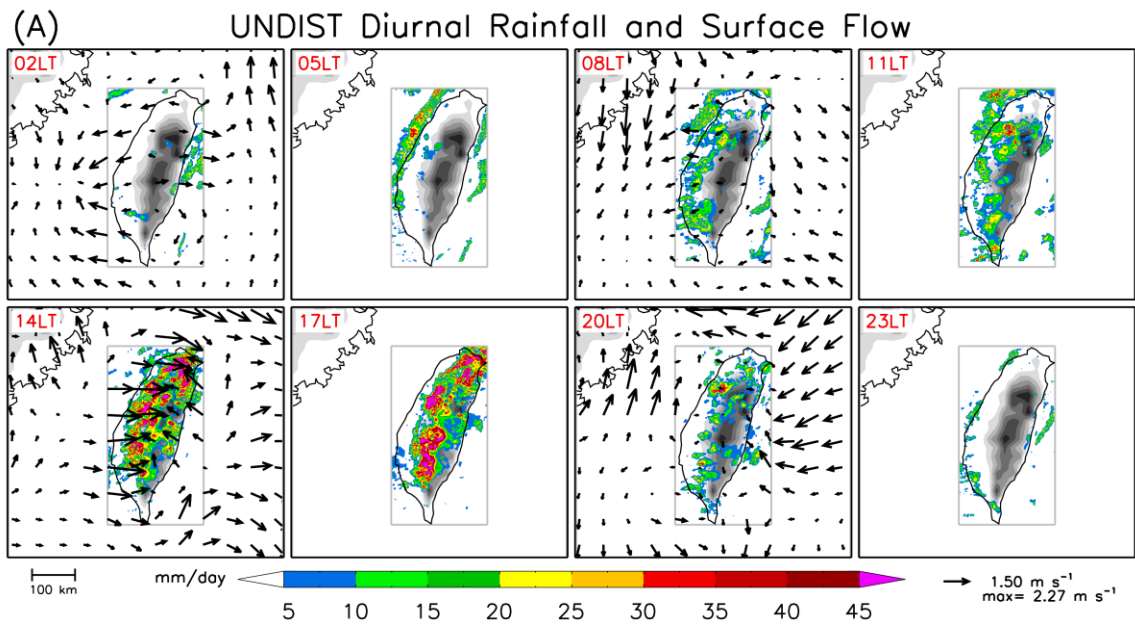


983

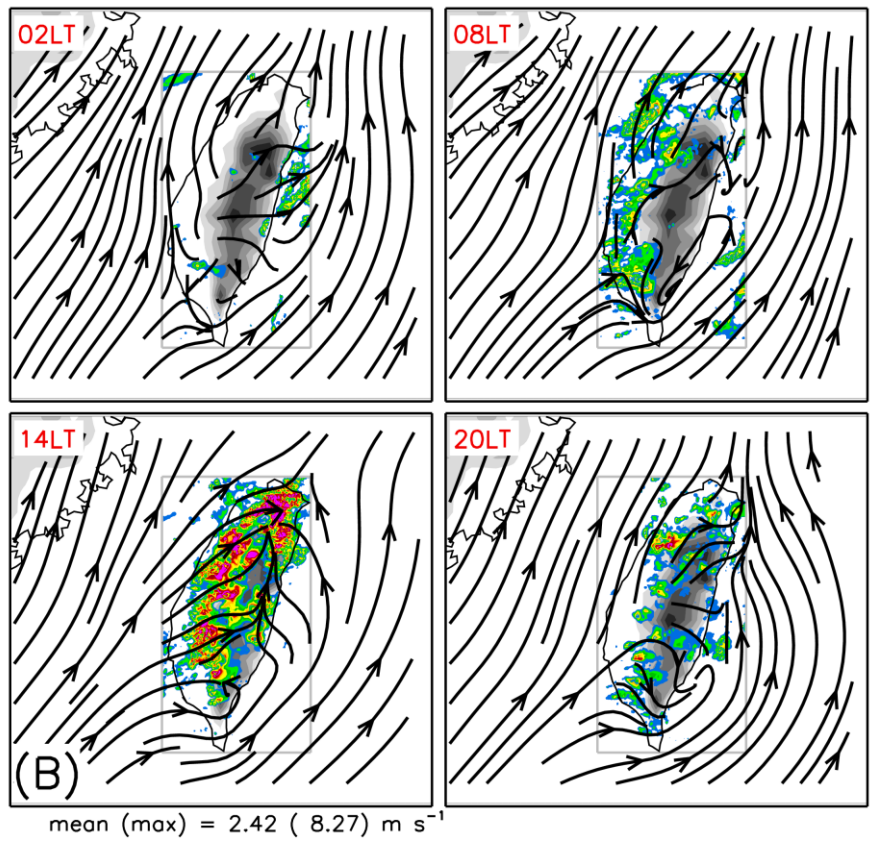
984

985 FIG. 8. UNDIST mean surface streamlines from INTERP (mean and maximum domain
 986 wind speed values provided at bottom) and rainfall (mm day⁻¹). QPESUMS rainfall is
 987 shaded (color scale at right), and TRMM rainfall is contoured at 5, 20, and 35 mm day⁻¹
 988 inside of the QPESUMS domain (gray rectangle) and shaded surrounding it. The red “X”
 989 marks Dongsha Island sounding station. Terrain is gray-shaded as in Fig 1.

990



991



992

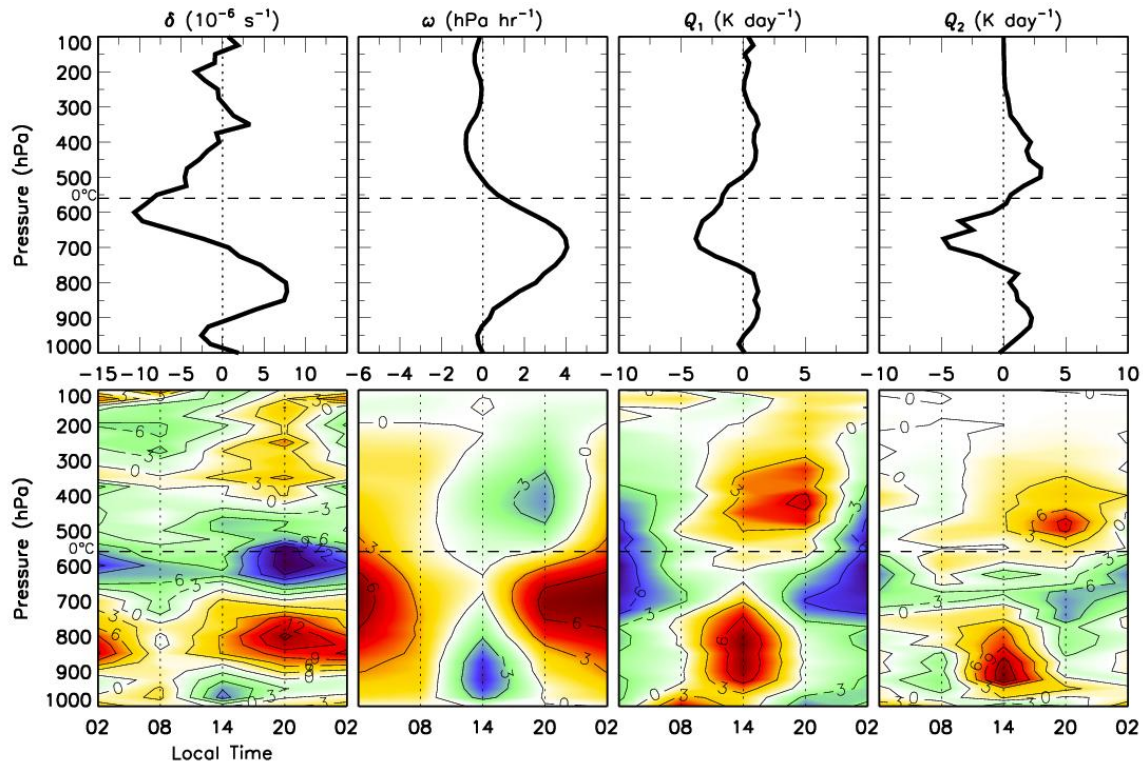
993

994 FIG. 9. (a): UNDIST six-hourly diurnal surface flow anomalies (m s⁻¹; reference vector

995 and maximum value provided at bottom-right) with three-hourly UNDIST composite

996 QPESUMS rainfall (mm day^{-1} ; scale at bottom). (b): UNDIST six-hourly diurnal
997 composite surface streamlines (mean and maximum domain values provided at bottom-
998 left) with QPESUMS rainfall [shaded according to the color bar in (a)]. LT is indicated
999 in the upper-left of each panel.

1000



1001

1002

1003 FIG. 10. UNDIST composite vertical profiles from INTERP averaged over Taiwan in

1004 mean (top) and diurnal composite (bottom) form (six-hourly sampling). From left to

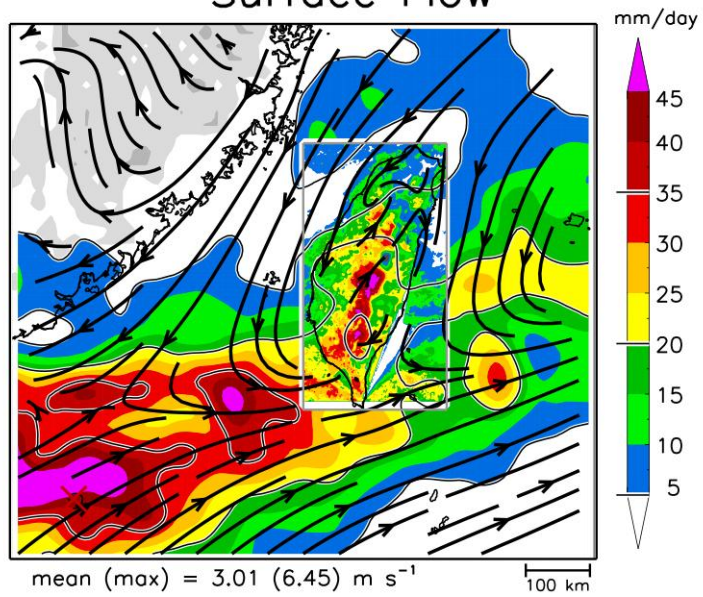
1005 right: δ (10^{-6} s^{-1}), ω (hPa h^{-1}), Q_1 (K day^{-1}), and Q_2 (K day^{-1}). The 0°C level is dashed.

1006 Abscissae are mean values (top) and LT (bottom). 02-LT values are repeated in diurnal

1007 profiles for continuity.

1008

DIST Mean Rainfall and Surface Flow

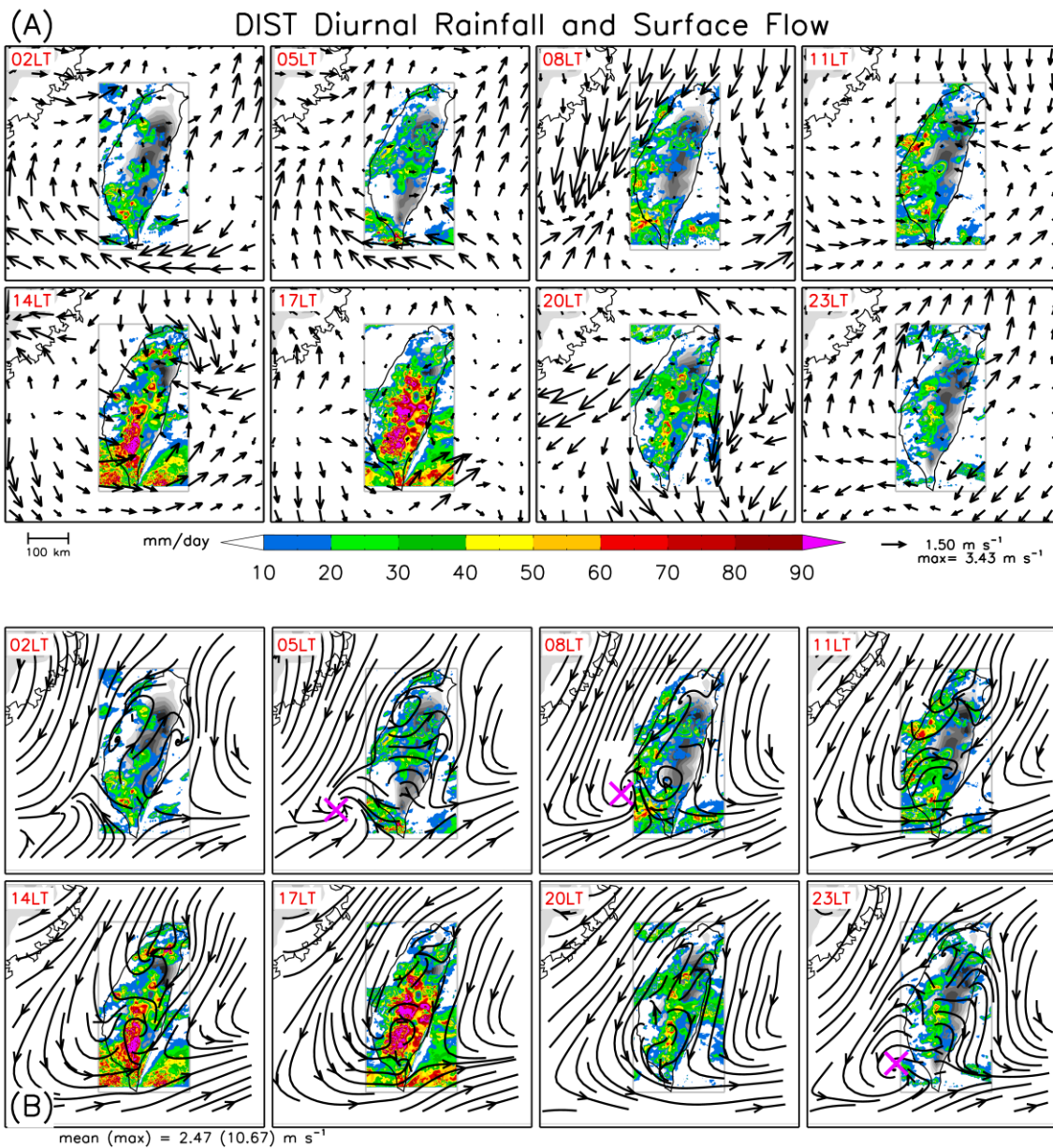


1009

1010

1011 FIG. 11. As in Fig. 8 except for DIST.

1012



1014

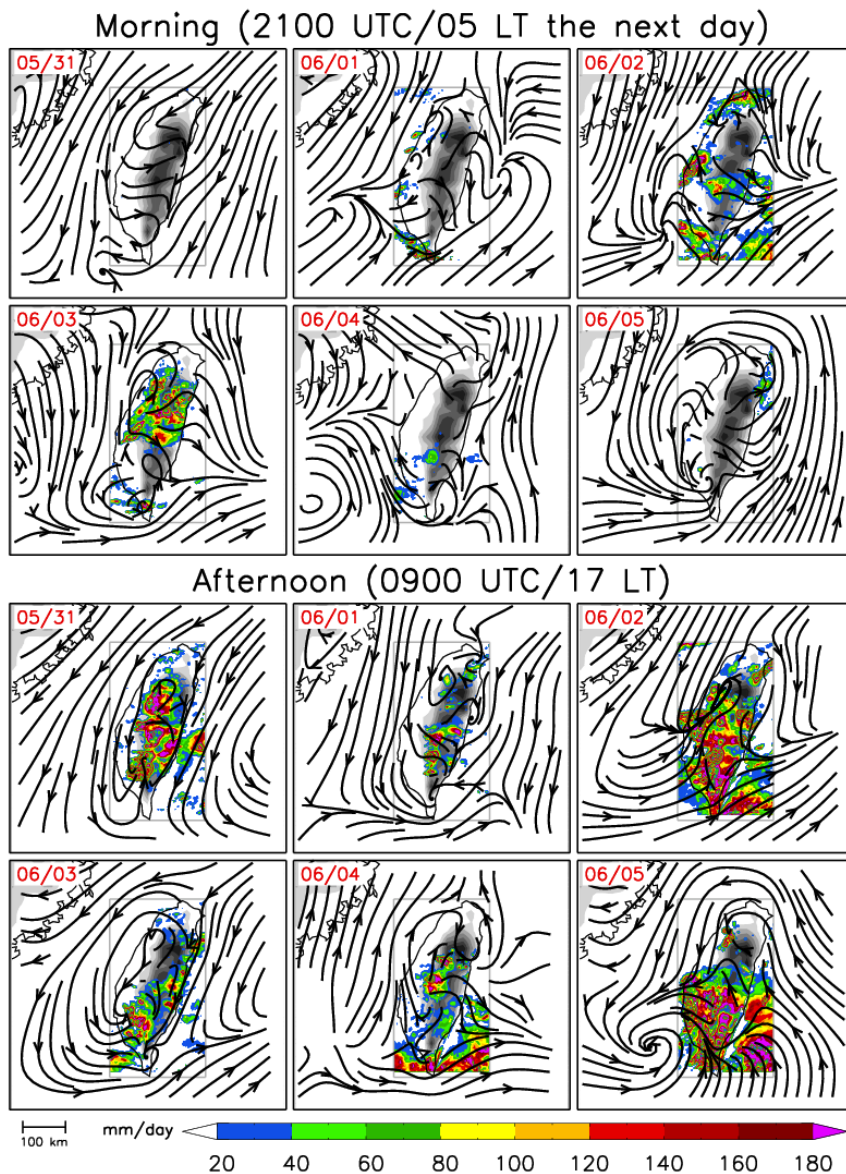
1015

1016 FIG. 12. As in Fig. 9 except for DIST. Note that the rainfall scale is doubled relative to

1017 Fig. 9. Also, diurnal flows are provided at three-hourly frequency during DIST since it

1018 coincided with the EOP. The magenta “X” in (b) marks a circulation center.

1019



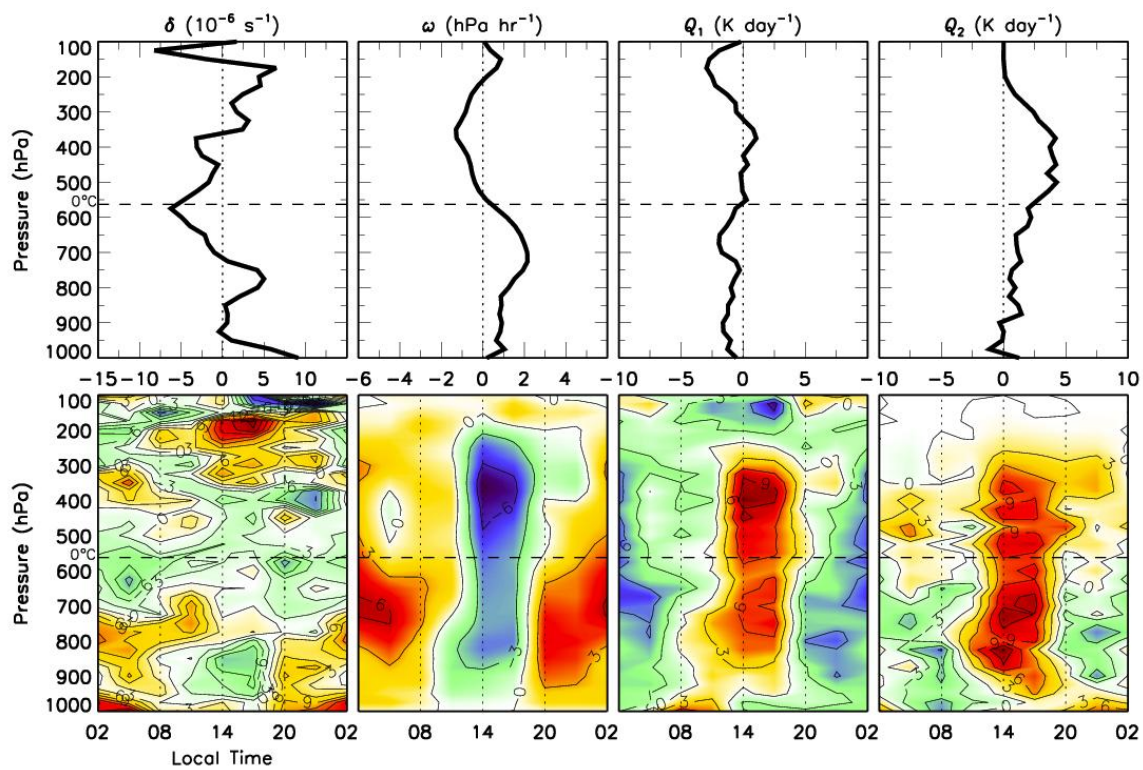
1020

1021

1022 FIG. 13. Surface streamlines and QPESUMS rainfall (mm day^{-1} ; shaded) for morning
 1023 (2100 UTC; 05 LT the next day) and afternoon (0900 UTC; 17 LT) on 31 May–5 June.

1024 Dates are indicated at the top-left of each panel, which pertain to UTC time.

1025

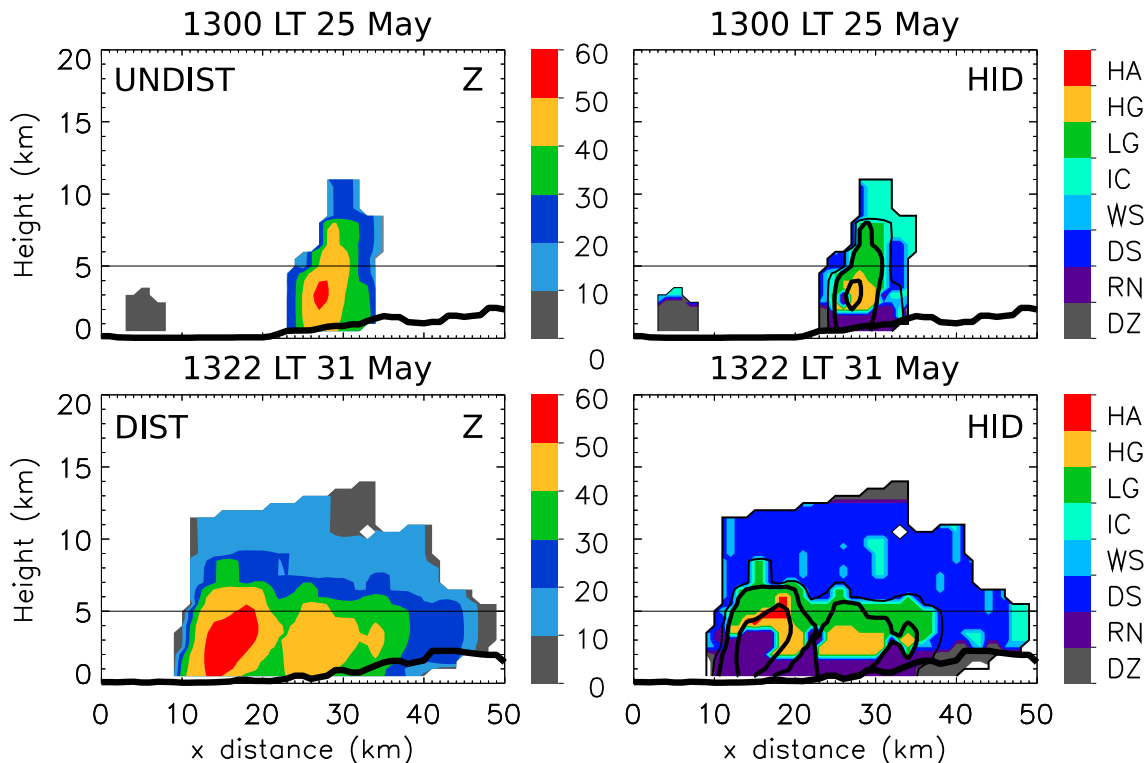


1026

1027

1028 FIG. 14. As in Fig. 10 except for DIST (with three-hourly sampling).

1029



1030

1031

1032 FIG. 15. West-to-east radar cross sections for UNDIST (1300 LT 25 May; top) and

1033 (1322 LT 31 May; bottom). Cross sections follow the transects shown in Fig. 1

1034 (UNDIST: southernmost transect; DIST: northernmost transect). Abscissa axis is

1035 distance from S-Pol radar (km), elevation is on ordinate axis (km), surface elevation is

1036 contoured in a thick black line, and the approximate 0°C level is indicated by the thin

1037 horizontal line at 5 km. Shown are reflectivity (dBZ; shaded; left panels) and

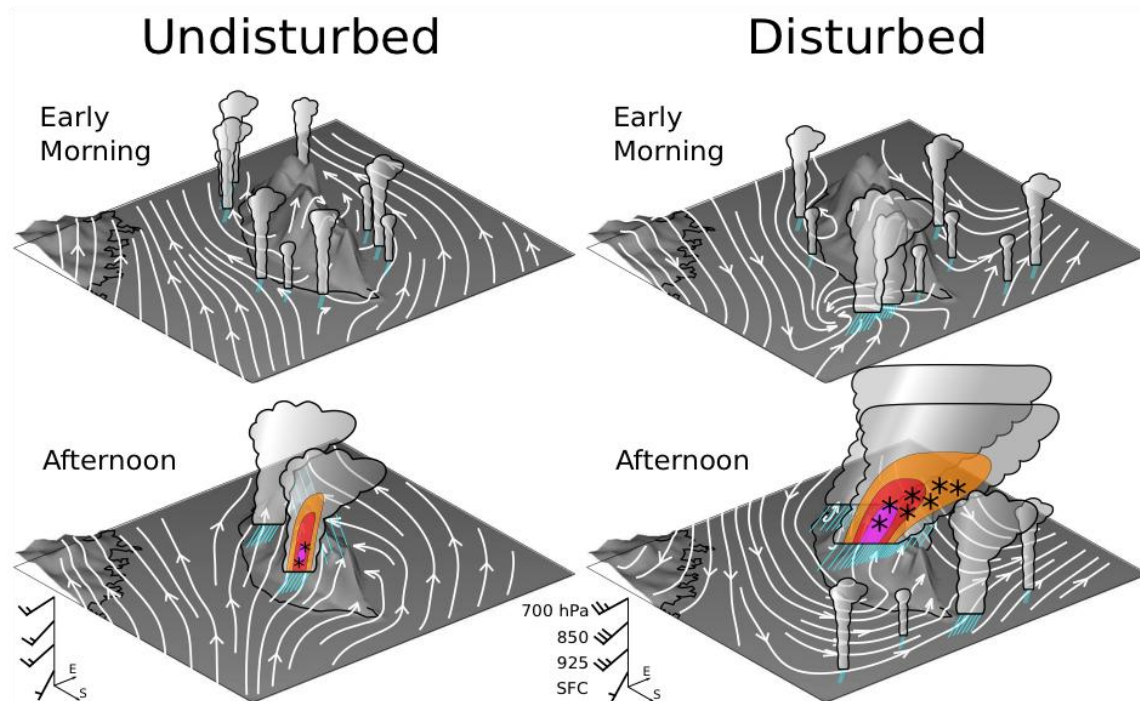
1038 hydrometeor identification (HID; shaded; right panels), with reflectivity contoured at 0,

1039 30, 40, and 50 dBZ (with 40- and 50-dBZ contours thickened). HID categories are

1040 drizzle (DZ), rain (RN), dry snow (DS), wet snow (WS), vertical ice (IC), low-density

1041 graupel (LG), high-density graupel (HG), and hail (HA).

1042



1043

1044

1045 FIG. 16. Schematic depiction of the diurnal cycle looking northeast over Taiwan during

1046 the two SoWMEX/TiMREX (2008) periods analyzed in this study. The undisturbed

1047 period (left; 22–29 May) was characterized by relatively uniform southwesterly

1048 impinging flow, large-scale subsidence, and a dry mid/upper-troposphere over Taiwan.

1049 During the disturbed period (right; 31 May–4 June), a surface Mei-yu front was situated

1050 in the northern SCS, the impinging southwesterly flow overriding the front was stronger

1051 and moister than UNDIST, and afternoon rainfall in Taiwan was heavier. Precipitation

1052 cores are schematically depicted to exemplify characteristics of afternoon deep

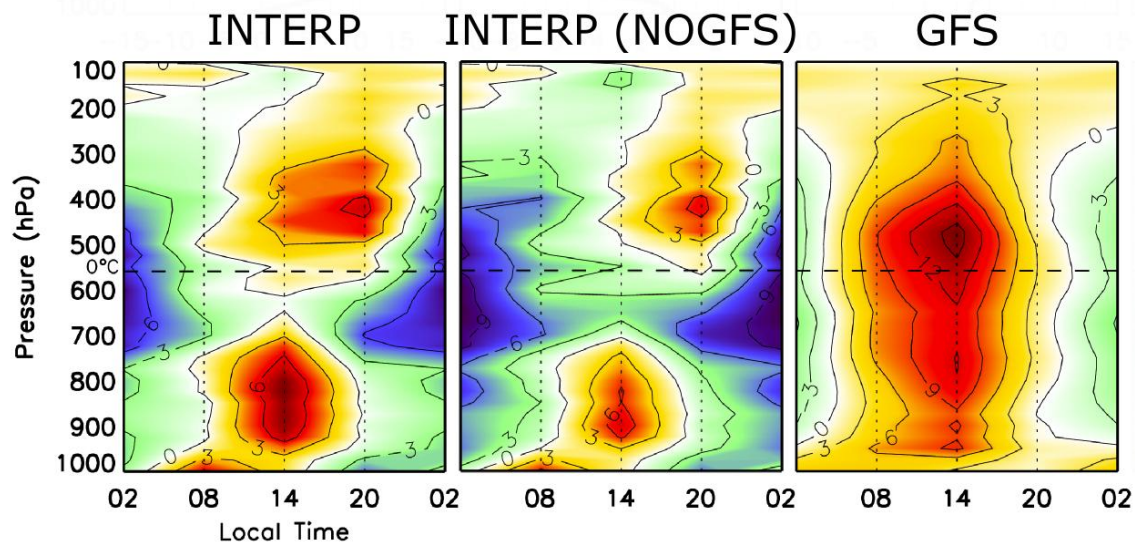
1053 convection along the western-coastal plains and windward slopes. Orange, red, and

1054 magenta shading indicates radar reflectivity exceeding 30-, 40-, and 50-dBZ,

1055 respectively. Asterisks represent ice hydrometeors. The blue lines indicate rainfall.

1056 Surface streamlines are based on 02- (05-) LT and 14- (17-) LT diurnal composites for

1057 morning and afternoon during UNDIST (DIST), respectively. Wind profiles are based on
1058 UNDIST and DIST mean soundings from Dongsha Island (location indicated in Fig. 8;
1059 half and full barbs denote 2.5 and 5 m s⁻¹, respectively). Vertical scale is exaggerated to
1060 emphasize terrain, and wind profiles and schematic clouds are not to scale.
1061



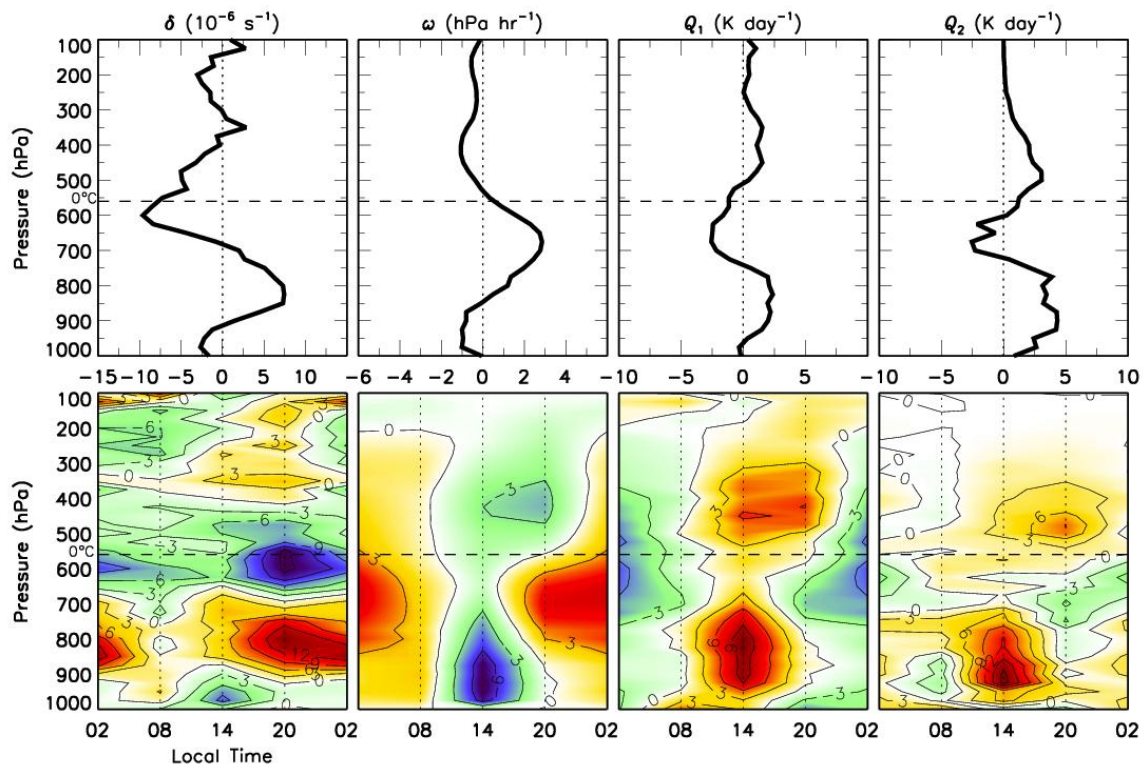
1062

1063

1064 FIG. A1. UNDIST diurnal composite vertical profiles of Q_1 averaged over Taiwan from

1065 INTERP (left), INTERP (excluding GFS data points; middle), and GFS (right).

1066



1067

1068

1069 FIG. A2. As in Fig. 10 except fields are averaged over western Taiwan (dividing line

1070 indicated in Fig. 1).